

# A Quasar Catalog with Simultaneous UV, Optical and X-ray Observations by *Swift*

Jian Wu<sup>1,4</sup>, Daniel Vanden Berk<sup>2</sup>, Dirk Grupe<sup>1</sup>, Scott Koch<sup>1</sup>, Jonathan Gelbord<sup>1</sup>,  
Donald P. Schneider<sup>1,3</sup>, Caryl Gronwall<sup>1,3</sup>, Sarah Wesolowski<sup>2</sup> and Blair L.  
Porterfield<sup>1</sup>  
jwu@astro.psu.edu

## ABSTRACT

We have compiled a catalog of optically-selected quasars with simultaneous observations in UV/optical and X-ray bands by the *Swift* Gamma Ray Burst Explorer. Objects in this catalog are identified by matching the *Swift* pointings with the Sloan Digital Sky Survey Data Release 5 quasar catalog. The final catalog contains 843 objects, among which 637 have both UVOT and XRT observations and 354 of which are detected by both instruments. The overall X-ray detection rate is  $\sim 60\%$  which rises to  $\sim 85\%$  among sources with at least 10 ks of XRT exposure time. We construct the time-averaged spectral energy distribution for each of the 354 quasars using UVOT photometric measurements and XRT spectra. From model fits to these SEDs, we find that the big blue bump contributes about  $\sim 0.3$  dex to the quasar luminosity. We re-visit the  $\alpha_{\text{ox}}-L_{2500 \text{ \AA}}$  relation by selecting a clean sample with only type 1 radio-quiet quasars; the dispersion of this relation is reduced by at least 15% compared to studies that use non-simultaneous UV/optical and X-ray data. We only found a weak correlation between  $L_{\text{bol}}/L_{\text{Edd}}$  and  $\alpha_{\text{UV}}$ . We do not find significant correlations between  $\alpha_{\text{x}}$  and  $\alpha_{\text{ox}}$ ,  $\alpha_{\text{ox}}$  and  $\alpha_{\text{UV}}$ , and  $\alpha_{\text{x}}$  and  $\log L(0.3-10 \text{ keV})$ . The correlations between  $\alpha_{\text{UV}}$  and  $\alpha_{\text{x}}$ ,  $\alpha_{\text{ox}}$  and  $\alpha_{\text{x}}$ ,  $\alpha_{\text{ox}}$  and  $\alpha_{\text{UV}}$ ,  $L_{\text{bol}}/L_{\text{Edd}}$  and  $\alpha_{\text{x}}$ , and  $L_{\text{bol}}/L_{\text{Edd}}$  and  $\alpha_{\text{ox}}$  are stronger amongst low-redshift quasars, indicating that these correlations are likely driven by the changes of SED shape with accretion state.

*Subject headings:* quasars: general — catalogs — ultraviolet emission — X-rays

---

<sup>1</sup>Department of Astronomy & Astrophysics, Pennsylvania State University, 525 Davey Lab, University Park, PA, 16802, USA

<sup>2</sup>Department of Physics, Saint Vincent College, 300 Fraser Purchase Road, Latrobe, PA, 15650

<sup>3</sup>Institute for Gravitation and the Cosmos, The Pennsylvania State University, University Park, PA 16802

<sup>4</sup>College of Information Sciences and Technology, The Pennsylvania State University, University Park, PA 16802

## 1. Introduction

Variability is a ubiquitous phenomenon of quasars (e.g., Matthews & Sandage 1963; Smith & Hoeffleit 1963; Gaskell & Klimek 2003; Vanden Berk et al. 2004; Wilhite et al. 2005, 2006; Meusinger et al. 2011) and has been observed in radio, infrared, UV/optical, X-ray and even  $\gamma$ -ray bands (e.g., Kovalev et al. 2002; Rieger & Aharonian 2008; Sakata et al. 2010; Park et al. 2010; Grupe et al. 2010).

While variability provides considerable information on the size scales of the quasar central engine and can be utilized to estimate the mass of the central super massive black hole (e.g., Peterson et al. 2004), it is a significant source of scatter in multi-wavelength correlations. Clearly, when fluxes of variable sources measured in different wavebands at different times are combined, the combined spectral shape may not be representative of the spectral shape at a specific time. It is therefore essential to take simultaneous observations when determining multi-waveband properties in order to understand the true spectral shape.

The dispersion in multi-waveband correlations produced by variability can be estimated. For example, there is evidence that at least 60% of the dispersion of the Baldwin Effect and at least 75% of the  $\text{EW}(\text{C IV})-\alpha_{\text{ox}}$  relation can be attributed to variability (Wu et al. 2009). However, a large multi-waveband program of simultaneous observations to verify that the dispersions of various relations can be reduced has not yet been performed. In this work, we will use simultaneously observed UV/optical and X-ray data to study quasar SEDs.

The *Swift* Gamma-ray Burst (GRB) Explorer (Gehrels et al. 2004) includes co-aligned X-ray and UV/optical detectors. The X-ray telescope (XRT; Burrows et al. 2005) is an imaging spectrometer that covers the 0.3–10 keV band. The Ultraviolet Optical Telescope (UVOT; Roming et al. 2005) provides photometry in six bands from  $\sim 1928 \text{ \AA}$  to  $\sim 5468 \text{ \AA}$ . By default, XRT and UVOT are operated simultaneously. Because *Swift* is primarily a GRB mission, there are few quasars that were specifically targeted for observations. However, due to the relatively large fields of view (FOVs) of both the UVOT and the XRT, a large number of serendipitous sources, including quasars, are observed. The Sloan Digital Sky Survey (SDSS; York et al. 2000) Data Release 5 (DR5;

Adelman-McCarthy et al. 2007) quasar catalog (Schneider et al. 2007) contains 77,429 optically-selected quasars in  $5,740 \text{ deg}^2$ ; the UVOT FOV is  $17' \times 17'$ , so there is a density of approximately one SDSS quasar per UVOT field. We have matched the *Swift* pointings from launch to June 2008 ( $\sim 3.5$  years) with the SDSS DR5 quasar catalog, to examine the properties of quasars observed simultaneously in UV and X-ray light.

Catalogs using similar strategies were constructed by Tueller et al. (2008) and Grupe et al. (2010). Our work is unique in terms of the selection criteria and sample size. The sample in Tueller et al. (2008) contains 153 hard X-ray (14–195 keV) selected local AGNs with a mean redshift of  $\sim 0.03$ . Because hard X-ray photons more easily penetrate gas and dust than UV/optical and soft X-ray photons, this study provides a more homogeneous sample of quasars than those based on UV/optical and soft X-ray bands. Using this sample, Winter et al. (2009) estimated the fraction of “Hidden” AGNs (Ueda et al. 2007) in the local universe to be  $\sim 24\%$ . The sample by Grupe et al. (2010) contains 92 soft X-ray selected AGNs with redshifts ranging from 0.002 to 0.349. Due to their selection criteria, objects in this sample are X-ray bright Type 1 AGNs with few Seyfert 1.5 objects (e.g., Mkn 841; see Wilkes et al. 1999). Their selection criteria are not biased for or against RL AGNs (about 10% of AGNs are RL). Using this sample, Grupe et al. (2010) constructed composite AGN SEDs with simultaneous observations from *Swift*. By fitting these SEDs with two different models, they attempted to constrain AGN bolometric corrections (BCs). They found a significant correlation between UV and X-ray spectral indices, namely  $\alpha_{\text{UV}}$  and  $\alpha_{\text{X}}^1$  for AGNs with  $\alpha_{\text{X}} > -1.6$ . Because their sample contains a large fraction of narrow line

---

<sup>1</sup>The spectral indices are defined as  $f_{\nu} \propto \nu^{+\alpha}$  in this work.

Seyfert 1 (NLS1) galaxies, they were also able to examine differences between broad line Seyfert 1 (BLS1) galaxies and NLS1 galaxies in terms of the  $\alpha_{\text{UV}}-L_{\text{bol}}/L_{\text{Edd}}$  relation.

As a result of the detection limits in their selected wavebands, both of the above studies are limited to nearby AGNs and relatively small sample sizes. We find 1034 SDSS quasars within  $20'$  of *Swift* pointings, which is almost an order of magnitude larger than either of these samples.

One of the prominent features in the AGN SED is the big blue bump (BBB) in the extreme UV (EUV) energy band, which is believed to be primarily produced by thermal emission from an accretion disk (e.g., Shields 1978). Because of strong Galactic and (possibly) intrinsic extinction, it is almost impossible to observe this wavelength region. This feature is likely, however, to be an important contributor to quasar bolometric luminosity. Based on the observed data in UV/optical and X-ray bands, we can place some constraints on the flux contribution of this feature. Grupe et al. (2010) were able to constrain the BBB using their sample of  $\sim 100$  AGNs at low redshift  $z < 0.4$ . In contrast, over 50% of the quasars in our sample are at  $z \gtrsim 1$ , thus, we will be able to better constrain the BBB feature.

It should be emphasized that we are not repeating the global SED work of Elvis et al. (1994) and Richards et al. (2006). We are attempting to use simultaneously acquired data to constrain the BBB. This component, because of the lack of observational data, is usually represented as a power-law connecting a UV flux point, such as  $2500 \text{ \AA}$ , to an X-ray point, such as  $2 \text{ keV}$  (e.g., Richards et al. 2006). The slope determined by these two points is defined as  $\alpha_{\text{ox}}$  (Tananbaum et al. 1979),

$$\alpha_{\text{ox}} = 0.3838 \log \left[ L_2 \text{ keV} / L_{2500 \text{ \AA}} \right] \quad (1)$$

which is used to characterize the spec-

tral hardness between the UV and X-ray bands (e.g., Avni & Tananbaum 1982, 1986; Anderson & Margon 1987; Wilkes et al. 1994; Vignali et al. 2003; Strateva et al. 2005; Steffen et al. 2006; Just et al. 2007). The expression above follows the notation convention in Just et al. (2007), so  $L_{2500 \text{ \AA}}$  is the monochromatic luminosity at  $2500 \text{ \AA}$  in  $\text{ergs s}^{-1} \text{ Hz}^{-1}$ . A long-standing problem with the measurement of  $\alpha_{\text{ox}}$  is that it is difficult to obtain simultaneous measurements of an object in the X-ray and UV/optical bands. Source variability introduces scatter into measurements of  $\alpha_{\text{ox}}$ . Our simultaneous observations remove this noise.

This paper is organized as follows. In Section 2, we describe the observations and data processing; in Section 3, we present our data processing results, including the UV/optical light curves, and the composite SED for each quasar; in Section 4, we present our final catalog; in Section 5, we select a sample of quasars from this catalog to study the dispersion of the  $\alpha_{\text{ox}}-L_{2500 \text{ \AA}}$  relation and other correlations. In Section 6, we summarize this catalog and our conclusions. Throughout this work, we adopt the following cosmology:  $\Omega_{\text{M}} = 0.3$ ,  $\Omega_{\Lambda} = 0.7$ ,  $H_0 = 70 \text{ km s}^{-1} \text{ Mpc}^{-1}$ .

## 2. Observations and Data Processing

Our quasar sample was compiled in the following steps.

1. Candidate objects for our catalog were selected as any SDSS DR5 quasar that lie within  $20'$  of the center of the *Swift* FOV in any pointing from launch through June 2008.
2. XRT data were processed to obtain X-ray count rates, spectra and spectral parameters.
3. UVOT data were processed to obtain UV and optical photometry.

4. UVOT photometry were supplemented with measurements at other wavelengths from published catalogs.
5. Quasar SEDs were constructed.
6. Additional parameters were calculated based on the SEDs of each quasar.

The raw sample is constructed by matching 3.5 years *Swift* pointings and the SDSS DR5 quasar catalog and contains 1034 objects. Fig. 1 shows the distribution of our quasar sample in the luminosity (represented by absolute magnitude  $M_i$ ) – redshift diagram. The distribution of our sample in this diagram is consistent with the SDSS DR5 quasar catalog.

## 2.1. XRT Data

We processed the XRT data using the task *xrtpipeline* (HEADAS version 6.10) from *FTOOLS* (Blackburn 1995). For each observation identified by an observational ID (hereafter OBSID), this routine stacks all available XRT snapshots (individual exposures with the same segment number) observed in photon counting mode and generates a composite *sky image* for each OBSID with an associated exposure map.

Source and background extraction regions are then defined for each quasar in the candidate list. The quasar coordinates are adopted from SDSS DR5 quasar catalog, which are accurate to  $\approx 1''$ . The source and background regions are circles with default radii of  $30''$  and  $120''$ , respectively. These circles are visually inspected in the deepest sky image. This ensures that the background does not include serendipitous X-ray sources. The position and size of the background region circle is adjusted so that it lies entirely within the field of view in all sky images covering this object. We exclude sky images in which the source region is not fully within the FOV or not covered by all individual exposures. We also discard sky images in which the source is severely

contaminated by nearby X-ray sources. Depending on the brightness of the X-ray source, the source region radius is adjusted to be large enough to ensure that the photon density at the border is at the same level as the background. We then enlarge the background region so that its radius is at least four times as large as the source region radius.

XRT data are prepared using standard *FTOOLS* packages. Event files for each OBSID are extracted and cleaned using *XSelect* (version V2.4a). *xrtmkarf* (version 0.5.6) is used to create an auxiliary response file (ARF) for each OBSID. The ARF file includes corrections for filter transmission, vignetting, effective area and point spread function (PSF). It also accounts for hot pixels and hot columns, which are masked out from data and decrease the effective exposure time. The response matrix file (RMF) we use is *swxpc0to12s0\_20010101v011.rmf*<sup>2</sup>

The total number of background-subtracted X-ray counts,  $N_{\text{Xph}}$ , is determined for each quasar by combining the counts measured in each sky image. This value is used to assign a quality flag to each object: *g* (good with  $N_{\text{Xph}} > 100$ ), *a* (acceptable with  $10 < N_{\text{Xph}} \leq 100$ ), *w* (weak with  $N_{\text{Xph}} \leq 10$ ), and *o* (out of FOV). In the candidate sample of 1034 quasars, 103 objects are flagged as good (*g*), 296 are flagged as acceptable (*a*)

<sup>2</sup>We noticed that this RMF file was intended for use with data taken from launch through 28 February 2007 only and that other RMFs are appropriate for data taken from March through August 2007 and for data taken since 30 August 2007. To test the sensitivity of our simple spectral models (described below) to the choice of response matrix, we fitted models to several high signal to noise sources using each RMF and found the impact upon the model parameters to be small: the spectral index changes by less than 0.02 and the intrinsic column density changes by no more than a few tens of percent. We therefore use a single RMF for simplicity and we choose the one for data taken prior to 28 February 2007 as the majority of our data is from this time interval and most of our sample members were observed at least in part before this date.

and 406 are flagged as weak ( $w$ ). The rest (229 objects) are flagged as  $o$  because they lack useful sky images.

Next, we produce summed event lists for the source and background regions, including all observations. From these we extract time-averaged spectra. We also generate the ARF file for the composite source spectra using *ad-darf* (version 1.2.6). The X-ray energy spectra are binned using *FTOOLS* task *grppha* (version 3.0.1).

The X-ray energy spectra are fit using *XSPEC* (Arnaud 1996; version 12.5.1n). The binning strategy and the statistical method we use are described in Table 1. Basically, we use  $\chi^2$  statistics and have at least ten spectral bins if  $N_{\text{Xph}} > 100$ . If  $N_{\text{Xph}} < 100$  we apply minimal binning to eliminate unoccupied spectral bins (this avoids having bins with negative background-subtracted fluxes) and use Cash statistics (Cash 1979). If  $N_{\text{Xph}} < 10$ , we only estimate flux or flux upper limits. For each object with  $N_{\text{Xph}} \gtrsim 10$ , we fit each X-ray spectrum with an absorbed power-law model. This model includes Galactic column density along the line of sight to the quasar  $N_{\text{H,G}}$  and possibly additional absorption intrinsic to it  $N_{\text{H,i}}$ . The values of  $N_{\text{H,G}}$  are fixed based upon the Leiden/Argentine/Bonn (LAB) survey of Galactic H I (Hartmann & Burton 1997; Kalberla et al. 2005). We define four variations of this model, depending upon whether the photon spectral index ( $\Gamma$ ) or  $N_{\text{H,i}}$  are allowed to vary as a fixed parameter. We define four variations of this model, depending upon whether this spectral index  $\alpha_x$  or  $N_{\text{H,i}}$  are allowed to vary (models A-D; Table 2). We visually inspect the fitting quality and apply the following rules to select the model that produces the best constraint and quality:

1. If  $N_{\text{Xph}} < 30$ , we use Model A. In this case, it is impossible to constrain the intrinsic absorption and the constraint on  $\alpha_x$  is poor ( $1\sigma$  uncertainty of  $\alpha_x$  is larger than  $\sim 0.5$ ). There-

fore, we fit only the flux levels and fix  $\alpha_x = -1$ , which is the average value of X-ray spectral index for RQ type 1 quasars (e.g., Nandra & Pounds 1994; Page et al. 2003, 2004; Young et al. 2009).

2. If  $30 \leq N_{\text{Xph}} < 100$ , we allow one additional free parameter, either  $N_{\text{H,i}}$  or  $\alpha_x$ , but not both:
  - If the intrinsic column density  $N_{\text{H,i}}$  is inconsistent with zero and well constrained, we choose Model D.
  - If  $N_{\text{H,i}}$  is consistent with zero, and  $\alpha_{\text{ox}}$  is reasonably well constrained ( $|\delta\alpha_x| < 0.5$ ), we choose Model B.
  - If neither of these criteria are met, we choose Model A.
3. In the case that  $N_{\text{Xph}} \geq 100$ , if  $\alpha_x$  is well constrained and the  $1\sigma$  lower bound of  $N_{\text{H,i}}$  is not consistent with zero, we use Model C. Otherwise, we follow Rule 2.

The visual inspection process is performed by three people and a consensus is reached to ensure objectivity. The number of quasars selected for each fitting model is shown in Table 2. Examples of the fitting are shown in Fig. 2.

Based on the spectral fitting results, we calculate a number of parameters, including the photon count rate, the observed and unabsorbed X-ray flux between 0.3 and 10 keV, and the monochromatic luminosity at 2 keV in the emitted frame. These values are included in the final catalog (see Section 4).

## 2.2. Weak X-ray Sources

We process weak X-ray sources (flagged as  $w$  in the final catalog) with  $N_{\text{Xph}} < 10$  separately because some are not significantly detected by XRT and we can only estimate their flux upper limits.

We apply the Bayesian method of (Kraft et al. 1991) to determine whether an X-ray source is detected or not. We define a source to be a non-detection if  $3\sigma$  confidence level lower limit is consistent with zero source counts. 98 out of 406 weak X-ray sources are detected by XRT.

For the detected sources, we fit Model A to determine  $F(0.3\text{--}10\text{ keV})$  and  $f(2\text{ keV})$ , which is the observed flux between 0.3 and 10 keV and the observed flux density at 2 keV. For undetected sources, we consider two cases. If the background-subtracted count rate is positive, we can use the *XSPEC* to apply Model A. This has the advantage of including the calibrations present in the ARF file, but the model will be fitted to the measured counts and not the upper limit and therefore must be rescaled. The flux upper limit is determined using

$$F_{\text{uplim}} = F_{\text{Xspec}} \frac{N_{\text{uplim}}}{N_{\text{Xph}}}. \quad (2)$$

in which  $N_{\text{uplim}}$  is the  $3\sigma$  source photon count upper limit.

If an undetected X-ray source has too few counts (typically  $N_{\text{Xph}} < 2$ ), *XSPEC* is unable to apply models to the data. In these cases we manually apply two corrections to convert the count limits into limiting count rates. The first correction is for vignetting. Vignetting is a reduction of the effective area of the telescope at off-axis positions. We adopt a vignetting function of  $V(\theta) = 1 - C\theta^2$ , where  $\theta$  is the off-axis angle in arcminute. The coefficient  $C$  varies with energy (Cusumano & the XRT Calibration Team, 2006; Kennea, private communication); here we adopt the value appropriate for 2 keV as it is representative and the uncertainty in our measurements is dominated by small number statistics. This correction is applied by reducing the effective exposure time by the vignetting factor, thereby increasing the count rate limit. The second correction is to account for the finite size of the aperture used to measure source

counts. We generate an ARF file appropriate for the size and position of the source extraction region. The output of this process includes a report of the fraction of the source fluence enclosed within the region; we divide the count limit by this fraction to apply the PSF correction. Finally, the vignetting- and PSF-corrected count rate limit is converted to limiting observed flux by using the tool *pimms* (Mukai 1993) together with the assumption of Model A. From this model we determine the absorption-corrected flux, flux density and monochromatic luminosity at 2 keV.

### 2.3. UVOT Data

Instead of using a pipeline to obtain a co-added event file as was done with the XRT data, we process each individual UVOT sky image for each object. The composite photometry is obtained by summing over photon counts from each individual image and dividing the sum by the total exposure time.

First, we must identify suspect and defective sky images. Because we are using serendipitous observations, it is inevitable that some sources are too close to the edge of the UVOT FOV<sup>3</sup>. The goal of this process is to exclude the low quality sky images so that the default source and background regions can be directly applied on good ones.

The source region is defined using a circle with a radius of  $3''$ , which is recommended in the UVOT photometric calibration (Poole et al. 2008). Since a  $5''$  radius aperture, which contains  $85.8 \pm 3.8\%$  of the PSF, was used for calibrating the UVOT, an aperture correction is applied to the data when running *uvotsource* (Poole et al. 2008). The inner and outer radii of the background regions are  $r = 27''.5$  and  $R = 35''.0$  respectively; this is the standard background region used

<sup>3</sup>Objects are not necessarily always within the FOV because the matching radius used to select the raw sample is larger than UVOT FOV and/or because UVOT was working under other modes.

to construct the first GRB afterglow catalog (Roming et al. 2009). The large difference between the source and background radii ensure that the background area is at least 50 times as large as the source region to provide an accurate background subtraction.

We then flag each sky image based on the position of the object in the image frame and the aspect keyword value. We only use images whose aspect values equal `DIRECT`. The other images (flagged as `-1`) do not have correct aspect corrections and may lead to inaccurate photometric results. The detailed image flagging strategy is tabulated in Table 3. We only accept UVOT images flagged with 0, 1 and 2.

Due to relatively small photon counts or positioning uncertainties, a fraction of object images are not symmetric or well aligned with the default source region circle with a radius of  $3''$ . It is necessary to co-align the quasar image with the center of the source region circle because the aperture correction process assumes a symmetric photon loss outside the pre-defined aperture. To co-align the locations, we extract a region of  $11 \times 11$  pixels (about  $5'' \times 5''$ ) centered on the SDSS quasar coordinates. If the total photon count inside this region is less than 20, we regard this image as “faint” and assign a flag of “1”. Even if a single image is regarded as “faint”, it may contribute to the total object counts when stacked with other images (e.g., Lehmer et al. 2007). If an image is not flagged as “faint”, we attempt to fit the source with a two-dimensional Gaussian profile the centroid of which is set to be free. The background is determined by averaging the photons inside the region centered at the SDSS coordinate and bounded by two squares with sizes of  $21 \times 21$  pixels and  $11 \times 11$  pixels. If the photon count inside the  $11 \times 11$  pixel region is less than three times that of the background level, this image is also treated as “faint” (flagged as “1”). Otherwise, we fit the  $11 \times 11$  pixel region with a 2-D Gaussian profile. The new Gaussian centroid is compared with the origi-

nal SDSS quasar coordinate. We denote their angular separation as  $\delta$ .

There are three categories of images.

- If  $\delta \leq 0''.618$ , the two coordinates are consistent and the default source region circle is used. This image is flagged as “0”.
- If  $0''.618 < \delta \leq 3''$ , this image is flagged as “2” and the source region circle is re-centered at the Gaussian centroid.
- If  $\delta > 3''$ , this image is flagged as “3”. This large offset could be caused by the unrecorded aspect problem, which requires manual correction or non-Gaussian photon distribution. Less than 1% of sky images are flagged as “3”, which are dropped.

In the next step, we define the default source and background regions for each object, and select the sky image with the longest passband central wavelength and the longest exposure, because, stellar contamination from host galaxies is larger in optical than in UV. If the V band is not available or its exposure is too short ( $\lesssim 100$  seconds), we examine the B band. If the B is unavailable, we check the U band, and then successively the UVW1, UVM2 and UVW2 bands. For each object, we attempt to exclude all stars, galaxies and bad pixels in the background annulus. If the source region is significantly contaminated or most of the background region must be masked, we remove this object from the UVOT analysis.

In most cases, the procedures above are sufficient to define a source and background region for all sky images. However, there remain a number of observations that require visual inspection. It is sometimes necessary to define a different background region to exclude the sky images in order to obtain acceptable photometry. For example, a number of images contain stellar ghost rings. Due to

differences of aspect and exposure time, the influence of these factors may vary for each sky image even for a given object. In addition, although the `ASPCORR` keyword may be set to `DIRECT`, the image may still suffer from uncorrected aspect problems so that a single point source may have multiple images or even smeared images. Consequently, it is necessary to visually inspect each sky image to perform the second order region customization and image selection. After the visual inspection process ( $> 50,000$  images), 3183 ( $\sim 1\%$ ) UVOT sky images were excluded from our UVOT image set.

We use `wotsource` (HEADAS version 6.10) to calculate photometry on *individual* sky images using the curves of growth from the *Swift* CALDB for the aperture correction model. The composite photometry uses the photon counts of all available images. For a given waveband, the mean magnitude is calculated as

$$\langle m \rangle = Z_{\text{pt}} - 2.5 \log \langle R_{\text{LSS}} \rangle \quad (3)$$

in which  $Z_{\text{pt}}$  is the zero-point magnitude (the magnitude when the count rate is 1 photon  $\text{s}^{-1}$ ). The values are taken from Table 6 of Poole et al. (2008).  $R_{\text{LSS}}$  is the source count rate with coincidence-loss, aperture, and large-scale sensitivity corrections applied. The associated uncertainty in this magnitude measurement is

$$\delta_{\langle m \rangle} = \sqrt{\Delta_{Z_{\text{pt}}}^2 + \left( \frac{2.5}{\ln 10} \langle R_{\text{LSS}} \rangle \right)^2 \Delta_{R_{\text{LSS}}}^2} \quad (4)$$

in which

$$\langle R_{\text{LSS}} \rangle = \frac{\sum R_{\text{LSS},i} \cdot T_i}{\sum T_i} \quad (5)$$

and

$$\Delta_{\langle R_{\text{LSS}} \rangle} = \frac{\sqrt{\sum (T_i \Delta_{R_{\text{LSS},i}})^2}}{\sum T_i} \quad (6)$$

where  $T_i$  is the exposure time in image  $i$ . We also calculate the flux density at the effective wavelength for each filter for each object

by multiplying the LSS photon count rate by the conversion factors in Table 10 (conversion from power-law spectra) of Poole et al. (2008).

The above equations can be applied to an individual sky image as well as a group of sky images. This process produces three measurements for each filter: photometry for each individual sky image, for all sky images in an OBSID, and for all OBSIDs of a filter.

A total of 675 objects in our sample are detected by UVOT.

### 3. Quasar SEDs

We classify objects in the database into four types based on data availability (see Table 4). In the description below, “useful data” includes both detections and non-detections.

- Type A contains 637 objects that have useful data from both UVOT and XRT. Among them, 345 are detected by UVOT *and* XRT.
- Type B contains the 38 objects that have useful data from UVOT but *not* XRT. These objects cannot be included in correlation analysis.
- Type C contains 168 objects that have only useful data from XRT but not UVOT. We will only create the XRT energy spectra for these objects.
- Type D contains 191 objects that are bereft of any useful data from UVOT or XRT. They are not included in the final catalog.

#### 3.1. Supplementary Data

As the object redshift increases, the UVOT wavebands are progressively shifted into the EUV band shortward of  $\text{Ly}\alpha$ ; as a consequence, UVOT data for some quasars cannot be used to measure the rest-frame UV power-law. The SDSS and 2MASS data, observed



at longer wavelengths, can be used to extend the available measurements to UV and optical bands in the quasars’ rest-frames. We supplement our UV photometry with the five bands (*ugriz*) from the SDSS DR5 quasar catalog and three bands (*J, H, Ks*) of the 2MASS (Cohen et al. 2003; Skrutskie et al. 2006) survey, when available. In the best cases, we have 14 photometric data points in UV/Optical wavebands: six from *Swift*/UVOT, five from SDSS, and three from 2MASS.

### 3.2. Initial SED Plots

The monochromatic luminosity corresponding to each UVOT filter can be easily computed after shifting the flux density to the quasar’s rest-frame. The frequency band widths are calculated by converting rest-frame FWHMs of corresponding wavebands.

The SDSS quasar catalog provides magnitudes that we must convert to flux densities. Instead of the *asinh* magnitude used in the general SDSS photometric measurements (Lupton et al. 1999), we convert the SDSS flux densities from corresponding band magnitude using the Pogson definition (Pogson 1857) which has a much simpler analytical expression  $m_1 = -2.5 \log f_1/f_0$ , where  $f_0$  is the zero-magnitude flux. The Pogson magnitude system deviates from the *asinh* system for faint objects. According to the *asinh softening parameters (b coefficients)* table in the SDSS DR5 photometric calibration document<sup>4</sup>, the difference between Pogson and *asinh* magnitudes is less than 1% for objects brighter than  $g = 22.60$  and  $u = 22.12$ . The majority of our objects are much brighter than the limit. The difference between the Pogson and *asinh* systems is therefore negligible. There is one object (SDSSJ122740.85+440604.7) whose B band magnitude is fainter than 22.60 and two objects (SDSSJ020316.37–074832.1, and SDSSJ133613.62+025703.8) whose U band

magnitudes are fainter than 22.12. They are all at high redshift ( $z > 2.5$ ) with extremely low X-ray photon counts ( $N_{\text{Xph}} < 10$ ), so they do not play significant roles statistically in the correlation analysis result. For wavebands in SDSS, we adopt the central wavelength and FWHM from Fukugita et al. (1996). For wavebands in 2MASS, we adopt the isophotal central wavelengths and bandwidths from Cohen et al. (2003).

For X-ray sources with less than 100 photon counts, we use a different binning strategy in *XSPEC* from the one presented in Table 1 to avoid large error bars. We use the command `setplot rebin` to re-bin the spectrum until each bin has a detection at least as large as  $1\sigma$  and no more than 100 bins may be so combined. Error types are set to `quad` which sums in quadrature the errors on the original bins. The `rebin` command only affects the plot appearance but not the fitting results (see Fig. 2 for examples), but produces a clear representation of the average flux levels and associated uncertainties. Because of the relatively large uncertainties in the X-ray energy spectrum, we calculate the lower and upper error bars of each flux point, instead of applying standard error propagation.

The *initial* quasar SEDs are generated based on all available UV/optical photometric data points and X-ray energy spectra. Before shifting into the rest-frame, we apply Galactic reddening corrections to all available wave band flux densities using the standard  $E(B - V)$  dependent extinction curve (Fitzpatrick 1999). Values of  $E(B - V)$  are calculated following Schlegel et al. (1998). Some examples of quasar SEDs are presented in Fig. 3.

These initial SEDs cannot be used for SED fitting for two main reasons.

- Broad emission lines can contribute significantly to broad band filter measurements, which may lead to incorrect SED shapes. For example, the band covering

<sup>4</sup>[http://www.sdss.org/dr5/algorithms/fluxcal.html#asinh\\_table](http://www.sdss.org/dr5/algorithms/fluxcal.html#asinh_table)

Ly $\alpha$  can alter the UV slope by up to 0.2.

- The dates of the observation from SDSS, 2MASS, and *Swift* for a given object differ, often by several years in the rest-frame. The data may need to be shifted to mitigate the effect of variability.

### 3.3. Emission Line Correction

Emission line corrections can be performed by subtracting the broad line contribution based on their average equivalent width (EW) (e.g., Elvis 2012, in preparation). Because we have SDSS UV/optical spectra for all quasars, we use a more sophisticated method in which we convolve the response function  $R(\lambda)$  of each filter with the observed spectrum  $f_{\text{tot}}(\lambda)$  and the power-law only spectrum  $f_{\text{pl}}(\lambda)$  to calculate the emission line correction factor.

$$\text{EC} = \log \frac{F_{\text{tot}}}{F_{\text{pl}}} \quad (7)$$

in which

$$F_{\text{tot}} = \int f_{\text{tot}}(\lambda) R(\lambda) d\lambda$$

$$F_{\text{pl}} = \int f_{\text{pl}}(\lambda) R(\lambda) d\lambda$$

Because the quasar UV power-law usually extends from Ly $\alpha$  to  $\sim 5600 \text{ \AA}$  (e.g., Vanden Berk et al. 2001), we only need to perform emission corrections to filters covered within this wavelength range. However, low-redshift quasar spectra do not cover Ly $\alpha$  and high-redshift quasar spectra do not cover  $5600 \text{ \AA}$ . In these cases, the emission line corrections are performed based on the composite spectrum in Vanden Berk et al. (2001). Although the shape of the composite spectrum may not be exactly the same as the real spectra, the mean corrections are sufficient for power-law slope estimation.

To estimate the errors introduced by performing emission line corrections using the

composite spectra, we examine the emission line correction trends as a function of redshift for different filters and find that the emission line correction is typically less than 0.1 dex (see Fig. 4). The real spectrum corrections are generally distributed around the composite spectrum, meaning they are generally in agreement. To view their differences more clearly, we plot the distributions of differences between these two corrections,  $\Delta\text{EC} = \text{EC}_{\text{real}} - \text{EC}_{\text{composite}}$ , in Fig. 5 (only the SDSS  $g$  band and UVOT B band are displayed, but other filters are similar). These distributions indicate that on average, the composite spectrum emission line correction is consistent with the real spectrum emission line correction; the dispersion of these distributions are around 0.05 dex. Therefore, we apply a systematic uncertainty of 0.05 dex to photometry corrected using the composite spectra.

After emission line correction, the median photometric slope agrees well with the median spectroscopic slope in the UV band, with a value of  $-0.43$ . In the upper panel of Fig. 6, we plot these two slopes for objects with SED fits. Most data points are distributed along the line representing  $\alpha_{\nu,\text{ph}} = \alpha_{\nu,\text{sp}}$  with considerable scatter. We believe that this scatter is mostly caused by low redshift quasars (typically  $z < 0.8$ ) in which the  $2200 \text{ \AA}$  “line-free” rest-frame continuum point is not covered by SDSS spectra. In these cases, the uncertainty of the UV spectroscopic slope  $\alpha_{\nu,\text{sp}}$  may be larger than for high redshift quasar spectra. The value of  $\alpha_{\nu,\text{sp}}$  can be more accurately measured for objects at higher redshifts, which explains why the dispersion of  $\alpha_{\nu,\text{ph}} - \alpha_{\nu,\text{sp}}$  is much smaller (*bottom panel*, Fig. 6). In the description of correlation and regression analysis, we consistently use  $\alpha_{\text{UV}}$  to represent  $\alpha_{\nu,\text{ph}}$  because the data used to fit the slope is taken simultaneously with the X-ray data.

### 3.4. Photometric Shift

The photometric data in SDSS and 2MASS are not observed simultaneously with the *Swift* UVOT data, so quasar variability can make flux comparisons uncertain. To make best use of these data, we must create some *pseudo*-simultaneous data points by shifting the observed flux levels to be consistent with the *Swift* UVOT photometry, assuming the UV/optical SED shapes remain unchanged. With additional data points, we can place tighter constraints to UV slopes and luminosities while still, in some sense, maintaining the simultaneous property of the dataset. The photometric shift follows strategies described below (see Table 5 and Fig. 7).

1. Because all quasars have five simultaneous SDSS photometric measurements we always interpolate or extrapolate the SDSS photometry to obtain fluxes at the UVOT filter effective wavelengths, then shift all SDSS and 2MASS photometry to match UVOT. Because there is no overlap between the 2MASS and UVOT bands, it is impossible to shift 2MASS photometry separately so we use the same amount of shift as the SDSS data. The 2MASS photometry is only used for a few high redshift quasars so the time difference between 2MASS and SDSS data will not affect the UV spectral slope for a majority of objects in our sample.
2. We prefer to match in the UVOT U band. The *Swift* U band is very close to the SDSS *u* band, which significantly reduces uncertainties introduced by interpolation or extrapolation. The U band, being bluer than the V and B bands, is also less contaminated by host galaxy light.
3. If *Swift* U band photometry is unavailable, we interpolate the SDSS *u* and *g* bands to match the *Swift* B band. If

neither the U nor the B band is available, we interpolate the SDSS *r* and *g* band to match the *Swift* V band.

4. If none of U, B, or V bands is available, we extrapolate the SDSS *g* and *u* band to match one of the UVW1, UVM2 or UVW2 bands, using the available UVOT filter with the longest effective wavelength. Matching these filters is only done as a last resort; the significant extrapolation required inevitably introduces considerable photometric uncertainties. Furthermore, these three bands frequently lie in the Lyman forest where the quasar SED suffers from severe intrinsic and intervening absorption (e.g., Rauch 1998). The continuum in this spectral region cannot be approximated as a single power-law.
5. When selecting the matching filters, we require the SDSS filters and the UVOT filters to *both* fall in the UV range (between Ly $\alpha$  and 5600 Å) or within the EUV range, simply because the UV power-law cannot be extended to EUV region.

Examples of photometric shifting results are presented in Fig. 8.

### 3.5. Error Analyses

For UVOT photometry, we adopt the photometric uncertainties produced by *uvot-source* and perform error propagation assuming these errors follow a Gaussian distribution. The uncertainties of the SDSS and 2MASS fluxes are calculated based on magnitude uncertainties in the SDSS DR5 quasar catalog. The frequency bandwidths plotted on the SED are converted from the corresponding FWHM of each filter.

For the XRT data, we use the parameter uncertainties produced by the *XSPEC error* command. Because the X-ray photon counts

follow a Poisson distribution, which is unsymmetric, we calculate the upper and lower error bars separately.

### 3.6. SED Models

Because of the deficiency of the EUV data, the exact quasar bolometric luminosities strongly depends on the model used to fit the BBB. Traditionally, emission in this “gap” is represented by a power-law continuum with a slope  $\alpha_{\text{ox}}$  (e.g., Richards et al. 2006). In this work, we consider a model which provides an upper limit to the flux of the BBB in the canonical case. This shape is inspired from the presence of a soft X-ray excess over a flat X-ray component reported by Arnaud et al. (1985) in *EXOSAT* spectra of Seyfert 1 galaxy Mkn 841 and further studied by Walter & Fink (1993) and Gierliński & Done (2004). The latter study found that this soft X-ray excess can be well fit by a black body of energy 0.1 – 0.2 keV. This result motivates us to *constrain* this feature using a “bump” shape. In the following context, this model will be called the *exponential decay model* (hereafter EXP model). In addition, we use another model that directly connects the high energy limit of the UV power-law and the lower energy limit of the X-ray power-law at 0.3 keV. We call it the *triple power-law model* (hereafter TPL model). In either model, total flux is the result of a UV and an X-ray component.

$$f_{\nu,\text{tot}} = f_{\nu,\text{UV}} + f_{\nu,\text{X}}. \quad (8)$$

**EXP model** In this model, the two components are

$$f_{\nu,\text{UV}} = 10^{\beta_{\text{UV}}} \nu^{\alpha_{\text{UV}}} e^{(-h\nu/kT_{\text{B}})^{\gamma_{\text{UV}}}} \quad (9)$$

$$f_{\nu,\text{X}} = 10^{\beta_{\text{X}}} \nu^{\alpha_{\text{X}}} e^{(-h\nu/kT_{\text{X}})^{\gamma_{\text{X}}}} \quad (10)$$

The UV component is a power-law multiplied by an exponential decay term. The power-law slope  $\alpha_{\text{UV}}$  and scale factor  $\beta_{\text{UV}}$  are obtained by fitting photometric data points covered in

the UV region (from 5600 Å to Ly $\alpha$ ). Canonically  $\alpha_{\text{UV}} \approx -0.4$  (e.g., Vanden Berk et al. 2001). The combination of exponential and power-law terms create a “bump” in the EUV region. The value of  $\gamma_{\text{UV}}$  controls how quickly the flux decays given a value of  $T_{\text{B}}$  which is obtained from the SED fitting. We fix  $\gamma_{\text{UV}}$  to be 1.5 so that at  $\nu < \nu(\text{Ly}\alpha)$  the contribution from the exponential term is negligible and the total curve agrees well with the UV power-law given the best fit of  $T_{\text{B}}$ . For example, if we adopt  $\gamma_{\text{UV}} = 1$  (e.g., Grupe et al. 2010), a typical value of  $T_{\text{B}} \sim 4$  Ryd from the SED fitting produces a discrepancy between the UV power-law and the total SED curve by  $\sim 0.1$  dex at  $\nu(\text{Ly}\alpha)$ .

The X-ray component is also a power-law multiplied by an exponential decay term. The power-law slope  $\alpha_{\text{X}}$  and scale factor  $\beta_{\text{X}}$  are obtained by fitting the X-ray energy spectra using *XSPEC*. The X-ray decay energy  $T_{\text{X}}$  is fixed at 0.3 keV. We adopt  $\gamma_{\text{X}} = -8/3$  which assumes neutral hydrogen absorption (Longair 1992).

We emphasize that both of the UV and X-ray components are only mathematical expressions. Specifically, the value of  $T_{\text{B}}$  does not reflect the accretion disk temperature. Our goal is to place a reasonable upper limit to the strength of the BBB which contributes a significant fraction of the bolometric luminosity (e.g., Mathews & Ferland 1987; Zheng et al. 1997; Laor et al. 1997; Telfer et al. 2002; Shang et al. 2005). Therefore, the specific mathematical form is not important.

Because the XRT observes photons between 0.3 and 10 keV, these measurements are shifted to a higher rest energy range for high redshift quasars, i.e., we lack the soft X-ray data points for these objects. This affects our SED fitting because if we only fit the observed data points, the decay energy of the bump will be shifted to a higher energy band as the redshift becomes higher, which leads to additional flux contribution. To solve this prob-

lem, we supplement artificial data points by extending the X-ray power-law from the minimum energy of the real data down to 0.3 keV. We use 0.3 keV as the lowest energy for the X-ray power-law based on previous X-ray studies of quasars. These investigations found that the X-ray power-law can extend from  $\sim 0.1$  keV to  $\gtrsim 10$  keV (e.g., Turner & Pounds 1989; Laor et al. 1997; George et al. 2000; Page et al. 2005; Young et al. 2009). We then fit all the data points with this SED model using the Levenberg-Marquardt algorithm, leaving  $T_{\text{B}}$  the only free parameter. The median value of  $T_{\text{B}}$  is 5.96 Ryd.

**TPL model** In this model, the UV and X-ray power-laws are fit in the same way as the EXP model. Instead of multiplying each power-law with an exponential decay term, we simply connect the UV power-law at  $\text{Ly}\alpha$  and the X-ray power-law at 0.3 keV and denote the slope as  $\alpha_{\text{UVX}}$ . The distribution of  $\alpha_{\text{UVX}}$  is presented in Fig. 9.

In a canonical situation, i.e.,  $\alpha_{\text{UV}} = -0.4$  and  $\alpha_{\text{x}} = 2$ , the EXP model generates a bump in the EUV region which produces an upper limit while the TPL model yields a lower limit of the strength of the BBB. This simple analysis may not apply to strong X-ray absorption quasars. An example is shown in the first SED plot in Fig. 10. In this case, the absorption leads to a flat UV slope in addition to low X-ray emission in soft X-ray band. In these cases, the EXP model does not produce a “bump” but a “dip” in the EUV region and the corresponding integrated bolometric luminosity is not reliable. These quasars are flagged as “red” and will not be included into our cleaned sample defined below. Examples of fitted SEDs using these two models are presented in Fig. 10.

### 3.7. Bolometric Luminosity and Black Hole Mass

To obtain black hole masses, we measure broad emission line widths with SDSS spec-

tra. We employ the same software package used in previous SDSS spectral analyses (e.g., Wu et al. 2009; Vanden Berk et al. 2011, in preparation). The Galactic reddening corrections to all the spectra are performed using the extinction curve of Fitzpatrick (1999). Values of  $E(B - V)$  are calculated following Schlegel et al. (1998). We use three components to fit a spectrum: a single power-law in the UV band (between the  $\text{Ly}\alpha$  emission line and  $\sim 5500 \text{ \AA}$ ), the small blue bump, the UV iron template from Vestergaard & Wilkes (2001) and the optical iron template from Véron-Cetty et al. (2004). Each broad emission line is fit by a single or multiple Gaussian profiles. To ensure that our software package produces consistent results with previous studies, we compare our black hole masses to these in Shen et al. (2008b).

Following Shen et al. (2008b), we adopt different black hole estimators depending on quasar redshifts. At  $z < 0.7$ , we use  $\text{H}\beta$  plus  $l_{\lambda}(5100 \text{ \AA})$ , at  $0.7 < z < 1.9$ , we use  $\text{Mg II}$  plus  $l_{\lambda}(3000 \text{ \AA})$ , and at  $z > 1.9$ , we use  $\text{C IV}$  plus  $l_{\lambda}(1350 \text{ \AA})$ . The black hole mass is calculated using the following equation (Shemmer et al. 2006; Shen et al. 2008b)

$$\log M_{\text{BH}} = a + b \log(\lambda L_{\lambda}) + 2 \log \text{FWHM} \quad (11)$$

in which  $M_{\text{BH}}$  is in solar mass  $M_{\odot}$ ,  $\lambda L_{\lambda}$  is in  $10^{44} \text{ ergs s}^{-1}$ , and FWHM is in  $\text{km s}^{-1}$ . The two coefficients,  $a$  and  $b$ , in this equation, are  $(a, b) = (0.66, 0.53)$  for quasars with  $z < 0.7$ ,  $(a, b) = (0.505, 0.62)$  for quasars with  $0.7 < z < 1.9$ , and  $(a, b) = (0.672, 0.61)$  for quasars with  $z > 1.9$  (see Table 6; McLure & Jarvis 2002; McLure & Dunlop 2004; Vestergaard & Peterson 2006).

For comparison purposes, we calculate the bolometric luminosity using the wavelength-dependent bolometric correction (BC) factors by Richards et al. (2006) which are obtained using the composite SED for a sample of SDSS DR3 quasars (Abazajian et al. 2005; Schneider et al. 2005), so that  $L_{\text{bol,SDSS}} =$

BC  $\cdot \lambda_\lambda$ . These are bolometric luminosities *without* using simultaneous observations and does not include the BBB component, which differs from the bolometric luminosity we obtained by SED integration.

We then compare some important correlations and distributions with Shen et al. (2008b). The black hole masses vs. bolometric luminosities of 923 quasars are plotted in Fig. 11<sup>5</sup>. The locations of these quasars are consistent with the locations of quasars in Fig. 11 of Shen et al. (2008b), indicating that most quasars are accreting at a sub-Eddington level, i.e.,  $0.1 < L_{\text{bol}}/L_{\text{Edd}} < 1$ . The few quasars that fall above  $L_{\text{bol}}/L_{\text{Edd}} = 1$  (they are accreting at super-Eddington level) are narrow line Seyfert 1 (NLS1) galaxies (Shen et al. 2008a; Grupe et al. 2010). The median values of  $\log \text{FWHM}/(\text{km s}^{-1})$  are 3.62, 3.63 and 3.75 for H $\beta$ , Mg II and C IV, respectively, which are consistent with Shen et al. (2008b). By comparing the FWHM calculated using both of H $\beta$  and Mg II or Mg II and C IV we find a potential source of bias in the calculation of black hole masses as the C IV FWHMs are systematically larger than those of H $\beta$  and Mg II. However, we still use the black hole masses estimated by C IV because this offset is small compared to the dispersion of the black hole mass distribution.

We also calculate the bolometric luminosities by integrating the two SED models from 5600 Å to 20 keV. In general, emission in this region contributes the majority of the quasar luminosity for typical Type 1 quasars.

In Fig. 12, we show the differences between the bolometric luminosities measurements by integrating the two SED models, and the bolometric luminosities calculated using BC. The EXP model and the TPL model produce bolometric luminosities average higher and lower than the  $L_{\text{bol}}$  from the BC, respectively. Because the bump

emission from the EXP model is more sensitive to the UV and X-ray observed spectral shapes than the TPL model, it has a larger dispersion. A small fraction of the EXP models produces less bolometric luminosity ( $\log L_{\text{bol,EXP}} - \log L_{\text{bol,SDSS}} < 0$ ) than the TPL models. Some of these objects are quasars with strong intrinsic absorption (the black shaded area in Fig. 12). The reason why the TPL model produces less bolometric luminosity on average than the BC method is because the bolometric correction by Richards et al. (2006) includes the infrared wavebands, which contribute about 37% of the total flux. After correcting for contributions from this component, the entire histograms of both the EXP and the TPL models should move positively by  $\sim 0.2$  dex. Consequentially, the TPL model on average produces a bolometric luminosity consistent with that from the BC and the EXP model on average over produces  $L_{\text{bol}}$  by  $\sim 0.3$  dex.

#### 4. Catalog Description

Our final catalog contains 843 quasars with  $0.0129 \leq z \leq 4.5766$  and  $-30.24 \lesssim M_i \lesssim -22.01$ . There are 675 objects observed by UVOT, 805 observed by XRT and 637 observed by both UVOT and XRT. The X-ray detection rate of the entire catalog is  $\approx 60\%$ . Among objects in the catalog, 345 objects are *detected* by both UVOT and XRT, so that we are able to determine their SEDs from UV to X-ray bands. These objects constitute our parent sample to evaluate the flux contribution from the BBB. This catalog contains parameters directly measured from UVOT and XRT data and quantities derived based on these measurements such as black hole masses and bolometric luminosity. Columns in this catalog are described in Table 7. Comments for special individual objects in this catalog are listed in Appendix 7. Because the catalog contains 63 columns, we publish the full catalog in electronic format. In Table 8, we

<sup>5</sup>The others are not displayed because of low SDSS spectral quality.

represent ten columns of some objects in our catalog.

## 5. Correlation Analyses

In this section, we investigate the  $\alpha_{\text{ox}}-L_{2500 \text{ \AA}}$  relationship using a selected sample of Type 1 quasars from our catalog. This correlation has been described in a series of papers (Avni & Tananbaum 1982; Marshall et al. 1984; Tananbaum et al. 1986; Anderson & Margon 1987; Wilkes et al. 1994; Pickering et al. 1994; Avni et al. 1995; Vignali et al. 2003; Strateva et al. 2005; Steffen et al. 2006; Just et al. 2007); as quasars become more luminous, their SEDs from UV to X-ray bands become softer, i.e., less X-ray emission with respect to UV emission. In the study of 372 type 1 quasars in Just et al. (2007; hereafter J07), the UV/optical data are drawn from the SDSS DR3 quasar catalog (Schneider et al. 2005), IUE (Boggess et al. 1978; Kondo et al. 1989) and the COMBO-17 survey (Wolf et al. 2003) which covers the E-CDF-S (Wolf et al. 2004). The X-ray data are from *ROSAT*, *Chandra*, and *XMM-Newton* observations. Because the time between UV/optical and X-ray observations could span a time scale of years, quasar variability inevitably introduces scatters to the  $\alpha_{\text{ox}}-L_{2500 \text{ \AA}}$  relation. In this section, we investigate whether this scatter can be reduced by simultaneous UV and X-ray observations.

### 5.1. Sample Selection

In this work, we use 637 quasars with simultaneous observations by both UVOT and XRT. Because this sample has a relatively low X-ray detection rate ( $\sim 65\%$ , see below) we applied an X-ray exposure cut-off to the XRT observations. The goal is to obtain a homogeneous, optically-selected sample with a relatively high X-ray detection rate while retaining a sufficiently large sample size. The sample size and X-ray detection rate as a function of exposure cut-off is presented in Fig. 13.

The X-ray detection rate is  $\sim 65\%$  if we use the entire parent sample. These censored data can be handled by the ASURV software package (Lavalley et al. 1992), but the large fraction of non-detections makes the results unreliable. On the other hand, if we increase the exposure cut-off, the detection rate can rise to  $> 95\%$ , but only a few objects remain in the sample and the statistics are very poor. In this paper, we use two samples to study the  $\alpha_{\text{ox}}-L_{2500 \text{ \AA}}$  relation: the *large catalog* sample which contains *all* qualified quasars selected from the parent sample with no XRT exposure cut-off; and the *small catalog* sample which is derived from the *large catalog* sample except that we apply an XRT exposure cut-off of 10 ks. The large sample has a sample size of over 400 quasars; the small sample has a higher X-ray detection rate ( $\sim 85\%$ , see Table 10). In the following analysis, we supplement both of these samples with AGNs from Grupe et al. (2010), which contains data for 88 AGNs observed simultaneously by *Swift*<sup>6</sup>. We define this sample *supplemental sample* or the *G10* sample. The G10 sample is soft X-ray selected and is composed of low luminosity Type 1 AGNs at low redshifts ( $z \lesssim 0.4$ ). Because the G10 sample is selected in a different way from our sample, this sample is not merged with our samples, but is only used for comparison purposes.

The catalog parent sample is mixed with different types of quasars. To obtain a *clean catalog sample*, we exclude objects that fall into any of the four categories listed below. The quasar types are determined by exploring previously published studies and by calculating relevant quantities, e.g., radio loudness. The numbers of quasars excluded in each type are tabulated in Table 9. Because the G10 sample was not selected in the same way as our catalog sample, we only use them

<sup>6</sup>There are 92 objects in total in the Grupe et al. (2010) study, but 4 objects were not observed with UVOT photometry.

to represent simultaneously observed objects at relatively low redshift and low luminosity. Therefore, the exposure time cut-off is not applied to the G10 sample. The G10 sample is X-ray selected, so all objects are detected by XRT.

**RL quasars** They frequently have substantial X-ray flux from the radio jet, which leads to a higher  $\alpha_{\text{ox}}$  than those of radio quiet quasars (Worrall et al. 1987; Brinkmann et al. 2000).

We adopt the “radio loudness” ( $R^*$ ) defined by the ratio of monochromatic luminosities at rest-frame 5 GHz and 2500 Å (Stocke et al. 1992; della Ceca et al. 1994; Lu et al. 2007; Miller et al. 2009), e.g.,  $R^* = L_{5 \text{ GHz}}/L_{2500 \text{ Å}}$ .

For most of the quasars in the parent sample, we calculate the  $k$ -corrected  $L_{5 \text{ GHz}}$  from the 20 cm peak flux from the Very Large Array (VLA) FIRST Survey (Becker et al. 1995; White et al. 1997) listed in the SDSS DR7 quasar catalog, assuming an average value of radio spectral index  $\alpha_r = -0.5$  (e.g., Kellermann et al. 1989; Komossa et al. 2006; Lu et al. 2007).

For objects not detected by the FIRST survey (but still covered), we estimate radio luminosity upper limits using the sensitivity limit of the FIRST survey, which is 1 mJy. This provides upper limits of  $R^*$ . If  $\log R^* < 1$ , we classify this object as RQ. If  $\log R^* \geq 1$ , we check other resources of radio surveys, such as the NRAO VLA Sky Survey (NVSS; Condon et al. 1998).

For objects not covered by the FIRST survey, we examine 15' NVSS images for strong nearby radio sources. If we cannot confirm the quasar is RQ, we conservatively exclude it from the clean sample.

We preferentially adopt  $L_{2500 \text{ Å}}$  from SDSS spectral fitting results, unless 2500 Å is not covered, in which situation we use  $L_{2500 \text{ Å}}$  calculated from the SED fitting.

**Lensed quasar** The fluxes from these quasars are amplified, so these objects are removed from the clean sample (e.g., Just et al. 2007).

**Blazars** Blazars, including BL Lac objects and FSRQs, usually have large amplitude variations in UV/optical (e.g., Rani et al. 2010) as well as strong radio and X-ray emission (e.g., Beckmann et al. 2003; Padovani et al. 2007). As a result, the values of  $\alpha_{\text{ox}}$  can vary significantly over time. The UV/optical spectra of BL Lac objects usually have a featureless continuum without any emission lines (e.g., Blandford & Rees 1978; Kollgaard 1994; Plotkin et al. 2008; Abdo et al. 2010). Many of them are RL and their emissions are believed to be relativistically beamed from the jet (Urry & Padovani 1995). Although some FSRQs exhibit similar broad emission line features as Type 1 quasars, their radio emission is still beamed and variable. All objects classified as blazars are also excluded from the clean sample.

**Reddened quasars** Our sample contains a number of quasars with shallow UV/optical slopes and/or strong soft X-ray decline. The relatively flat UV/optical spectra are attributed to dust reddening (Richards 2001; Richards et al. 2003; Hopkins et al. 2004), although observations of individual objects suggest that some slopes could be intrinsically steep (e.g., Hall et al. 2006). Because the gas density of the AGN BLR is much higher and radiative transfer effects are not the same as in the low density regime (e.g., Hao et al. 2005), traditional approaches to correct reddening by the Balmer decrement cannot be applied for quasars. In this work, we only flag these objects and exclude them from the cleaned sample.

Following Richards et al. (2003), we use the relative color to define the “dust-reddened” quasars. The *relative color* is calculated by subtracting the median colors of quasars at the redshift of each quasar from its measured colors. As argued by Richards et al. (2003),



the quantity  $\Delta(g-i) = (g-i) - \text{Median}(g-i)_z$  is an excellent redshift-independent surrogate for the photometric spectral index. In Fig. 14, we plot  $\Delta(g-i)$  vs. redshift for all the objects in our raw catalog. Objects to the right of the dashed line are flagged as “dust-reddened” quasars. These quasars, which comprise 8.5% of the raw catalog, are excluded from our clean sample.

### Broad absorption line (BAL) quasars

BAL quasars are excluded from the clean sample because the emission line absorption is found to be associated with the continuum absorption in both of the UV/optical and the X-ray bands (e.g., Mathur et al. 1995; Brandt et al. 2000). This property can significantly affect the spectral indices and flux values obtained by fitting photometric data points, which produces inaccurate values of  $\alpha_{\text{ox}}$ . Most BAL quasars in the parent sample are identified in the BAL quasar catalogs by Trump et al. (2006) and Gibson et al. (2009). We found 50 BAL quasars in the parent sample; seven of them are also identified to be red quasars.

## 5.2. The $\alpha_{\text{ox}}-L_{2500 \text{ \AA}}$ Relation

In this section, we compare the dispersions of the  $\alpha_{\text{ox}}-L_{2500 \text{ \AA}}$  relation between the J07 sample and our cleaned catalog sample. We show that the dispersion can be reduced using simultaneous UV and X-ray observations. Because the exact values of the dispersion could be method-dependent, we use two methods in our analyses. We will present two sets of results based on both of the small and large cleaned catalog sample as well as for the combined sample.

Because our sample contains censored data, we use the ASURV software package (Lavalley et al. 1992) to perform statistical analysis. This package includes the Expectation-Maximization (EM; Dempster et al. 1977) and the Buckley-James (BJ; Buckley & James 1979) algorithms, which we can use

to perform linear regression and dispersion estimation. The methods differ in that the EM algorithm estimates the residual assuming a Gaussian distribution while the BJ algorithm assumes the Kaplan-Meier distribution. The correlation and regression results are tabulated in Table 11. We discuss the results and their implications below.

The clean catalog and the combined samples both exhibit strong correlations between  $\alpha_{\text{ox}}$  and  $L_{2500 \text{ \AA}}$ , although the absolute values of the correlation coefficients are slightly lower than the J07 sample. The relatively large fraction of undetected objects in the large clean catalog sample smears the correlation, but it is more evident in the small clean catalog sample with a higher X-ray detection rate.

The slopes ( $-0.16 \pm 0.02$  for the small sample and  $-0.15 \pm 0.01$  for the large sample) are both steeper than the J07 sample. The intercepts are also larger, but they are both consistent within  $2\sigma$  uncertainty. The combined sample has a shallower slope than the clean catalog sample; this change is caused by the G10 sample. The possibility that the  $\alpha_{\text{ox}}-L_{2500 \text{ \AA}}$  relation is non-linear is proposed in the study of Wilkes et al. (1994) and Anderson et al. (2003). As discussed by Wilkes et al. (1994), the difference in slopes is likely caused by the varying host galaxy contribution to the  $L_{2500 \text{ \AA}}$  measurement at low redshift. This may be the reason for the shallower slope of the G10 sample since no host galaxy contribution correction is applied<sup>7</sup>. Strateva et al. (2005) found that their sample does not offer significant evidence for a non-linear  $\alpha_{\text{ox}}-L_{2500 \text{ \AA}}$  relation. Although they obtained a shallower slope of  $-0.09 \pm 0.02$  for the low luminosity ( $\log L_{\text{UV}} < 30.5$ ) and  $-0.13 \pm 0.02$  for the high luminos-

<sup>7</sup>We do not correct for host galaxy light in our sample either, but since the majority of our objects are luminous quasars at higher redshift than G10, the host galaxy contamination is much smaller.

ity ( $\log L_{\text{UV}} > 30.5$ ) sample, they argue that the difference in slopes is likely an artifact of the addition of five outlier AGNs, which are probably X-ray-absorbed Seyfert galaxies at  $z < 0.22$ . From Fig. 15, we do not see suspected low luminosity “outliers”, but we still cannot exclude the possibility that the shallower slope is caused by host galaxy contamination. In addition, we also note that the J07 sample contains a number of the most luminous quasars with  $\log L_{\text{UV}} > 31.5$ , but excluding these high luminosity quasars does not reduce the slope significantly (see regression results of J07T<sup>8</sup> in Table 11). A careful removal of host galaxy contribution to the images is probably necessary for further checks, e.g., by using *GalFit* (Peng et al. 2002, 2010).

From Table 11, it is clear that the standard deviation of the clean catalog sample is smaller than the J07 sample by about 13%–19%. The large clean sample has the largest dispersion (BJ algorithm), which is comparable with the J07 sample, but this large dispersion is mostly caused by a large fraction of undetected X-ray sources. Using the EM algorithm, the J07 sample still has the largest dispersion among all samples. The small catalog sample exhibits a dispersion reduced even more by 18%–25%, compared with J07. In general, the combined sample has an even smaller intrinsic dispersion because the G10 sample has a higher degree of simultaneity.

The dispersion of the  $\alpha_{\text{ox}}-L_{2500 \text{ \AA}}$  relation does not exhibit a luminosity dependence (see Figure 7 of Just et al. 2007). From Fig. 15, we do not see the dispersion showing any evident dependence on luminosity (at least for X-ray detected quasars), either.

### 5.3. Correlations Between UV/optical and X-ray Spectral Indices

Previous studies found that AGNs with bluer optical/UV spectra have relatively

<sup>8</sup>The low luminosity sample  $\log L_{2500 \text{ \AA}} \leq 31$  in J07.

steeper X-ray spectra (Walter & Fink 1993; Grupe et al. 2008). Using simultaneously observed nearby AGNs, Grupe et al. (2010) found a mild correlation between  $\alpha_{\text{UV}}$  and  $\alpha_{\text{x}}$  (See Figure 10 of their paper). In Fig. 16, we plot  $\alpha_{\text{UV}}$  from UVOT photometric data vs. the X-ray spectral slope  $\alpha_{\text{x}}$  for objects from our clean catalog sample (objects whose  $\alpha_{\text{x}}$  were fixed to  $-1$  are excluded). The Spearman correlation coefficient for the data is  $\rho_s = -0.136$  ( $P_0 = 0.125$ ), which indicates a very weak correlation but the value of  $P_0$  indicates low confidence level<sup>9</sup>. As claimed by Grupe et al. (2010), the correlation between  $\alpha_{\text{UV}}$  and  $\alpha_{\text{x}}$  is primarily driven by BLS1 with  $\alpha_{\text{x}} > -1.6$ . By excluding NLS1 and  $\alpha_{\text{x}} < -1.6$  spectra objects from our sample, we find that the correlation coefficient  $\rho_s = -0.22$  with  $P_0 = 0.016$ , which still does not indicate a significant correlation.

To investigate whether the lack of this correlation in our sample is due to the wider range of redshifts compared to the Grupe et al. (2010) sample, we select the low-redshift counterparts from our sample with  $z < 0.4$ , marked in blue in Fig. 16. These objects exhibit a stronger correlation, with  $\rho_s = -0.468$  ( $P_0 = 0.058$ ). Although this subsample contains only 17 objects, we argue that this result is expected and due to changes of measured spectral slope in soft and hard X-ray bands. In the G10 sample, most AGNs are at low redshift so the rest-frame X-ray spectra cover both soft and hard X-ray bands. Because this sample is soft X-ray selected, objects in this sample usually exhibit strong soft X-ray emission with respect to hard X-ray emission, which is caused by the soft X-ray excess. The majority of our sample is composed of quasars with much higher redshifts, so the rest-frame X-ray spectra cover relatively less soft X-ray band. As a result,

<sup>9</sup>The null hypothesis here is that the correlation does not exist, so the lower  $P_0$  is, the more confident we feel on this correlation and vice versa.

the measured photon indices are mostly based on hard X-ray data.

We further investigate whether the correlation differences are due to the differences between the luminosity range in our sample and that of G10. As seen in Fig. 15, the G10 sample is composed mostly of low luminosity AGNs with a luminosity upper limit of  $\log L_{2500 \text{ \AA}} \sim 30.5$ . We select a subsample of quasars from the clean catalog sample with  $\log L_{2500 \text{ \AA}} < 30.5$  (green diamonds in Fig. 16) and found that the correlation coefficient is only 0.043 with a very low confidence level  $P_0 = 0.726$ . Therefore, our data do not support the argument that the differences between  $\alpha_{\text{UV}}-\alpha_{\text{x}}$  correlation found by Grupe et al. (2010) and in our work are due to luminosity differences, but more objects are needed to verify this.

#### 5.4. Correlation between $\alpha_{\text{ox}}$ and Spectral indices

Using the low redshift AGN sample, Grupe et al. (2010) found a correlation between  $\alpha_{\text{ox}}$  and  $\alpha_{\text{x}}$ , i.e., AGNs with softer X-ray spectra tend to be X-ray weak relative to UV band, which is consistent with the results of Atlee & Mathur (2009). In Fig. 17, we plot  $\alpha_{\text{ox}}$  vs.  $\alpha_{\text{x}}$  for 129 objects in our clean catalog sample. We do not see a significant correlation with  $\rho_s = -0.062$  ( $P_0 = 0.484$ ). Similar to the method described in Section 5.3, we select a subsample with  $z < 0.4$ , which is the low redshift counter part of the G10 sample. The  $\alpha_{\text{ox}}$  and  $\alpha_{\text{x}}$  of this subsample exhibit a strong correlation, although this subsample contains only 17 objects.

To see if the lack of correlation is due to redshift, we plot the high redshift ( $z > 1.5$ ) objects of the catalog sample in red. These objects are at a different location from the G10 sample with relatively higher values of  $\alpha_{\text{x}}$ . As we argued in Section 5.3, the measured value of spectral slope may depend on the rest-frame energy range. Because the ob-

served energy range is fixed, we do not see the soft X-ray energy spectra for high redshift quasars and thus photon indices measured for these objects suffer less from the soft X-ray excess.

We also display the low luminosity subsample ( $\log L_{2500 \text{ \AA}} < 30.5$ ) using diamonds in Fig. 17, which contains only eight objects. The subsample size is too small and we cannot decide if lack of correlation is related to the observed luminosity range.

Compared with the positive correlation found in Grupe et al. (2010), we plot the marginal linear correlation found by Young et al. (2009) in Fig. 17, which shows a *negative* correlation. The regression by Young et al. (2009) in general agrees with our data trend. The sample in Young et al. (2009) contains RQ quasars over a redshift range of  $z = 0.11-5.41$ , which is very similar to our sample. However, both the Atlee & Mathur (2009) and the G10 sample contain soft X-ray selected AGNs at low redshift. Because the fixed observed energy range, the spectral indices we measured for high redshift quasars represent the hard X-ray spectral shapes and are less affected by the soft X-ray excess which produce lower values of  $\alpha_{\text{x}}$ . The marginal correlation found in Young et al. (2009) is not seen in our sample is likely because they fit their spectral over the 0.5–10 keV band which covers less portion of the soft energy band and are less vulnerable to the soft X-ray excess. Therefore, the correlation found by Grupe et al. (2010) basically implies that AGNs with softer SEDs over the UV and X-ray bands tend to have stronger soft X-ray excess. This is consistent with the argument that the soft X-ray excess is a tail of the BBB in the EUV band, which originates from the thermal emission from the accretion disk. The lack of correlation in our sample and marginal correlation found by Young et al. (2009) implies that the hard X-ray generation process is relatively independent of the process producing the BBB photons.

Grupe et al. (2010) also found a correlation between  $\alpha_{\text{ox}}$  and  $\alpha_{\text{UV}}$ , which is not seen in our sample. The Spearman correlation coefficient is  $\rho_s = 0.166$  ( $P_0 = 0.014$ ). The low redshift subsample ( $z < 0.4$ ) contains only nine objects which reside at similar location as the G10 sample and appear to exhibit a strong correlation with  $\rho_s = -0.683$  ( $P_0 = 0.042$ ). However, the objects in our sample with higher redshifts cover a much wider range of  $\alpha_{\text{ox}}$  values.

The G10 sample is X-ray selected, so this sample will naturally include objects with stronger X-ray with respect to UV emission. Our sample is optically selected so it may contain objects with relatively weak X-ray with respect to UV/optical emission. It is clear to see from Fig. 15 that our sample contains objects with lower values of  $\alpha_{\text{ox}}$ . If we combine our sample with the G10 sample, we see a mild correlation between  $\alpha_{\text{ox}}$  and  $\alpha_{\text{UV}}$ , but with a large dispersion for high  $\alpha_{\text{UV}}$  objects.

### 5.5. Correlation Between $L_{\text{bol}}/L_{\text{Edd}}$ vs. Spectral Slopes

It has been reported that the Eddington ratio  $L_{\text{bol}}/L_{\text{Edd}}$  is correlated with  $\alpha_{\text{UV}}$ ,  $\alpha_x$ , and  $\alpha_{\text{ox}}$  (e.g., Grupe et al. 2010). Intuitively, this reflects that the accretion state affects the AGN spectral shape. Using the clean catalog sample, we find a mild correlation between the Eddington ratio and the UV spectral index (Fig. 19). The Spearman correlation coefficient is  $\rho_s = 0.35$  ( $P_0 < 10^{-3}$ ). The linear regression result is

$$\log L_{\text{bol}}/L_{\text{Edd}} = (1.194 \pm 0.302)\alpha_{\text{UV}} + (0.102 \pm 0.094) \quad (12)$$

In Fig. 19, we over plot the linear regression results for BLS1s (magenta dash dotted line), NLS1s (blue dash dotted line) and both (black dotted line). The BLS1 linear relation is clearly more consistent with our result because most objects in our sample are Type 1 quasars. We also distinguish objects in our sample at different redshifts but we do not see

any systematic offset for quasars at different redshifts. However, because the Eddington ratios used in Fig. 19 are calculated using the bolometric luminosity under the EXP model, the values of  $L_{\text{bol}}/L_{\text{Edd}}$  are not entirely independent of  $\alpha_{\text{UV}}$ . Thus, an independent measurement of  $L_{\text{bol}}/L_{\text{Edd}}$  is required to verify this correlation.

Compared to  $\alpha_{\text{UV}}$ , the value of bolometric luminosity is much less dependent on  $\alpha_x$  (Fig. 20). The Spearman correlation coefficient is  $\rho_s = -0.36$  ( $P_0 < 10^{-3}$ ) which indicates a mild correlation. We perform linear regression to all data points in our sample

$$\log L_{\text{bol}}/L_{\text{Edd}} = (-1.187 \pm 0.211)\alpha_x + (-1.740 \pm 0.175) \quad (13)$$

The slope is generally consistent with that found by Shemmer et al. (2008) ( $-0.9 \pm 0.3$ ) and shallower than the slope reported by Grupe et al. (2010) ( $-1.65 \pm 0.26$ ). In Fig. 20, we distinguish objects at different redshifts in different colors. Again, quasars at low redshift ( $z < 0.4$ ) have relatively lower values of  $\alpha_x$ , because of the soft X-ray excess. After excluding these objects from our clean sample, the correlation coefficient is  $\rho_s = -0.30$  ( $P_0 = 0.001$ ), and the linear regression slope is  $-0.88 \pm 0.61$ . The enhanced correlation for low redshift quasars indicates that the accretion state change causes the change of the accretion disk temperature. Specifically, higher accretion rate increases the disk temperature, which leads to a higher level of soft X-ray excess.

Grupe et al. (2010) also found a strong correlation between  $L_{\text{bol}}/L_{\text{Edd}}$  and  $\alpha_{\text{ox}}$ . This correlation was not seen in the sample of Shemmer et al. (2008). In Fig. 21, we see a very weak correlation between these two quantities with  $\rho_s = -0.16$  ( $P_0 < 10^{-3}$ ). By distinguishing quasars in different redshifts in colors, we notice that the strong correlation between  $L_{\text{bol}}/L_{\text{Edd}}$  and  $\alpha_{\text{ox}}$  stronger for low redshift quasars. Because of methods used in sample selection, the G10 sam-

ple consists of mostly X-ray bright AGNs, thus relatively higher value of  $\alpha_{\text{ox}}$ . Because of this bias, many UV/optical bright and X-ray normal/faint quasars are excluded. After including these quasars, the correlation becomes much less significant. Even by combining G10 sample with our sample, the correlation remains weak with significant scatter.

### 5.6. X-ray Slope versus Redshift and Luminosity

We do not find that the X-ray photon index  $\Gamma$  has any significant correlations with redshift, UV or X-ray luminosity (Fig. 22). The Spearman correlation coefficients are  $\rho_s = -0.14$  ( $P_0 = 0.003$ ) for redshift,  $\rho_s = -0.13$  ( $P_0 = 0.13$ ) for  $L_{2500 \text{ \AA}}$ , and  $\rho_s = -0.09$  ( $P_0 = 0.27$ ) for  $L_{2 \text{ keV}}$ . Adding the G10 sample does not make these correlations stronger. This result confirms previous studies with smaller or comparable samples (Page et al. 2004; Risaliti & Elvis 2005; Shemmer et al. 2005; Vignali et al. 2005; Kelly et al. 2007; Young et al. 2009).

## 6. Conclusions

We have compiled an optically selected quasar catalog with serendipitous and simultaneous UV/optical and X-ray observations with the *Swift* observatory. The catalog is generated by matching the  $\sim 3.5$  year *Swift* pointings from November, 2004 to June, 2008 to the SDSS DR5 quasar catalog. For each object, the sky images observed by either UVOT or XRT are carefully selected to ensure high image quality. We derive the composite UVOT photometry and XRT energy spectra by stacking all archival data to generate the deepest sky images. The resultant SEDs reflect the time-averaged shape of quasar emission with simultaneous observations at multi-wavebands. The catalog contains 843 objects. There are 637 objects ( $\sim 76\%$ ) that have UVOT and XRT observations, 168 objects ( $\sim 20\%$ ) that only have XRT data and 38

objects that only have UVOT data ( $\sim 4\%$ ). Among all the 675 objects with X-ray coverage, 460 ( $\sim 60\%$ ) are detected, which rises to 85% amongst source with at least 10 ks of XRT exposure time. We construct SEDs for all objects with both XRT and UVOT data. In this work, we focus on 637 objects with both X-ray and UV observations. We supplement UVOT photometry with SDSS and 2MASS data if available. All the photometric points are corrected for the effects of emission lines, and fluxes from SDSS and 2MASS are shifted to match the flux levels of *Swift* UVOT data.

We fit SEDs using the EXP and TPL models, attempting to constrain the flux contribution from the BBB. In most cases, the EXP models create a bump in the EUV region, producing an upper limit on the BBB emission, while the TPL model connects the SED points at 1216  $\text{\AA}$  and 0.3 keV, producing a lower limit on the BBB emission. After correcting for the contribution from IR emission, the TPL model produces bolometric luminosities consistent with those estimated using BCs from composite quasar SEDs, while the EXP model produces bolometric luminosities on average 0.3 dex higher than the TPL model.

We identify two clean samples (large and small) selected from our catalog, and supplement each sample with 88 nearby AGNs from Grupe et al. (2010). We re-visit the  $\alpha_{\text{ox}}-L_{2500 \text{ \AA}}$  relation presented by Just et al. (2007). We use the EM and Buckley-James methods to compare the intrinsic scatters of the  $\alpha_{\text{ox}}-L_{2500 \text{ \AA}}$  relationship of our and the J07 sample. These two methods consistently indicate that the dispersion based on our sample is reduced compared to J07 by 13% to 19% using the cleaned catalog sample and 18% to 25% using the combined sample.

Firmly establishing the  $\alpha_{\text{ox}}-L_{2500 \text{ \AA}}$  relation in AGNs is an important step toward understanding energy generation mechanisms

of AGNs. Our work has verified the correlation again, and has shown that the correlation is even tighter after reducing or eliminating scatter due to variability. An additional source of scatter in the correlation could be due to an intrinsic  $\alpha_{\text{ox}}-L_{2500 \text{ \AA}}$  relation, which may have a different slope for each quasar. In Fig. 7 of Vasudevan & Fabian (2009), they present simultaneously and non-simultaneously observed SEDs in the UV and X-ray bands. The dramatic difference between two SEDs for three of these objects indicates the variation of  $\alpha_{\text{ox}}$  with time for a given AGN. This variation then reflects the change of accretion state of the central engine and a different slope for an intrinsic and for a global relation would produce scatter around the global relation. In order to see the intrinsic  $\alpha_{\text{ox}}$  variation with  $L_{2500 \text{ \AA}}$  for an given AGN/quasar, it is necessary to gather long-term simultaneous observational data. In our future work, we will perform time-resolved UV/X-ray data analyses to selected targets from our catalog which was observed with high cadence, which will determine the contribution to the scatter of the global  $\alpha_{\text{ox}}-L_{2500 \text{ \AA}}$  relation from the intrinsic variations of X-ray with respect to UV emissions.

We also investigate correlations between spectral shapes in different wavebands and  $L_{\text{bol}}/L_{\text{Edd}}$ , and compare the results found in G10. Our low redshift ( $z < 0.4$ ) counterparts to the G10 sample verify significant correlations exist between  $\alpha_{\text{UV}}$  and  $\alpha_{\text{x}}$ ,  $\alpha_{\text{ox}}$  and  $\alpha_{\text{x}}$ ,  $\alpha_{\text{ox}}$  and  $\alpha_{\text{UV}}$ ,  $L_{\text{bol}}/L_{\text{Edd}}$  and  $\alpha_{\text{UV}}$ ,  $L_{\text{bol}}/L_{\text{Edd}}$  and  $\alpha_{\text{x}}$ ,  $L_{\text{bol}}/L_{\text{Edd}}$  and  $\alpha_{\text{ox}}$ , which physically implies that the accretion status plays a fundamental role in shaping the quasar SED between UV and soft X-ray band. This supports the argument that the BBB is produced by the disk emission and the soft X-ray excess is a result of thermal emission from accretion disk. However, for high redshift quasars, the measurement of X-ray spectral slope covers less soft energy band and is less affected by the soft X-ray excess. As a result, the cor-

relations between spectral shapes are much weaker after including high redshift quasars. This implies that the hard X-ray emission is relatively independent of the thermal emission on the accretion disk.

We received much assistance for this project from people at the *Swift* Mission Operation Center. Jamie Kennea helped us understand the XRT exposure maps; Pete Roming offered comments on the UVOT photometric calculations. We also received some helpful comments and discussions from Kim Page and Phil Evans. We also thank Bin Luo, Patrick Broos, Richard Wade, and Cristian Saez for their suggestions on this project. We also thank the referee for his/her useful comments which improves the quality of this paper. This project is financially supported by NSF grant AST06-07634 and NASA ADAP grant NNX09AC87G.

Funding for the SDSS and SDSS-II has been provided by the Alfred P. Sloan Foundation, the Participating Institutions, the National Science Foundation, the U.S. Department of Energy, the National Aeronautics and Space Administration, the Japanese Monbukagakusho, the Max Planck Society, and the Higher Education Funding Council for England. The SDSS website is <http://www.sdss.org/>.

The Institute for Gravitation and the Cosmos is supported by the Eberly College of Science and the Office of the Senior Vice President for Research at the Pennsylvania State University.

Swift is supported at PSU by NASA contract NAS5-00136.

## 7. Comments on Individual Objects

The following sources possess special spectroscopic or photometric features or have unusual classifications.

*SDSSJ021702.66–082052.3*. This is a flat spectrum radio quasar (FSRQ) cataloged by Massaro et al. (2009). The optical spectrum exhibits a featureless continuum with very weak Mg II  $\lambda 2798$  and H $\beta$  emission lines and a few narrow lines such as [O III]  $\lambda\lambda 4960, 5008$ .

*SDSSJ074110.70+311200.2*. This is an FSRQ (Liu & Zhang 2002; Healey et al. 2007).

*SDSSJ074625.86+254902.1*. This is a high redshift FSRQ (Massaro et al. 2009) with  $z = 2.979$  and an MeV blazar discovered by *Swift* (Sambruna et al. 2006; Tueller et al. 2008; Jolley et al. 2009) and thus in the BAT-selected AGN catalog by Winter et al. (2009). It is also observed by *Suzaku* (Watanabe et al. 2009). The UV spectrum contains broad emission lines such as Ly $\alpha$ , C IV  $\lambda 1549$  and C III  $\lambda 1908$ , which is unusual for a blazar.

*SDSSJ081331.28+254503.0*. This is a confirmed lensed quasar (Williams et al. 2008; Congdon et al. 2010; Inada et al. 2010).

*SDSSJ083148.87+042939.0*. This is an FSRQ with peak radio flux of  $\sim 1$  Jy. Its optical spectrum exhibits a featureless continuum with an extremely weak H $\alpha$  emission line.

*SDSSJ083740.24+245423.1*. This object is a blazar and classified as an FSRQ by Healey et al. (2007). The UV spectrum exhibits strong Mg II and C III  $\lambda 1908$  emission lines.

*SDSSJ090821.01+045059.4*. The Mg II emission line at  $\sim 2798$  Å is barely detected, H $\beta$  is extremely weak and the two nearby [O III] lines are quite prominent, indicating that the BLR is obscured and only the NLR is seen. This object has been identified as a strong radio source (e.g., Griffith et al. 1995) but the exact classification is not yet deter-

mined.

*SDSSJ092703.01+390220.8*. This is an FSRQ with a strong radio jet (Liu & Zhang 2002; Healey et al. 2007). The UV / optical spectrum also contains prominent Mg II  $\lambda 2798$ , H $\beta$  and H  $\gamma$  emission lines.

*SDSSJ094215.12+090015.8*. This is quasar with double-peaked H $\alpha$ . The FWHM of the broad component is extremely wide and reaches  $\sim 40,600$  km s $^{-1}$ , which is the broadest known (Wang et al. 2005). The broad H $\alpha$  suggests that the emission region is close to the black hole  $r \sim 80\text{--}100 r_g$  (Strateva et al. 2006).

*SDSSJ101405.89+000620.3*. This quasar is classified as a Seyfert 1.8 by Dong et al. (2005). The optical spectrum exhibits a strong and double-peaked H $\alpha$  line but a weak H $\beta$  line. The excess emission over the power-law around these two lines is likely to be contributed by host galaxy light.

*SDSSJ101541.14+594445.2*. This is a RL quasar exhibiting two pairs of radio lobes in an X-shape (Cheung 2007). The origin of the X-shape wings in this radio source is unclear.

*SDSSJ101810.98+354239.4*. This is an FSRQ (Healey et al. 2007).

*SDSSJ102738.53+605016.5*. The optical spectrum of this object exhibits extremely broad and double-peaked H $\beta$ , and is cataloged as a double-peaked emission line quasar by Wu & Liu (2004). They measured the FWHM of H $\beta$  of  $\sim 16,200$  km s $^{-1}$  and a black hole mass of  $\log(M_{\text{BH}}/M_{\odot}) = 9.649$ .

*SDSSJ103303.70+411606.2*. This is an FSRQ (Healey et al. 2007).

*SDSSJ121826.51+294846.5*. This object, also known as Mkn 766 and NGC 4253, is a local Seyfert 1.5 galaxy ( $z = 0.013$ ) and is resolved in the UVOT image. Because of the strong host galaxy contamination, it is difficult to isolate the AGN component. It is not included in our UVOT processing list. The X-ray spectrum is complicated; it cannot be fit by any model we described in Table 2.

This object was previously studied in detail in the *Swift* AGN catalog by Turner et al. (2006, 2007); Grupe et al. (2010).

*SDSSJ135516.54+561244.7*. This is a typical NLS1 (Zhou et al. 2006; Grupe et al. 1999, 2010).

*SDSSJ141927.49+044513.8*. This object has a featureless UV spectrum with a few narrow absorption lines. It is a BL Lac object in the catalogs of Collinge et al. (2005), Plotkin et al. (2008) and Massaro et al. (2009). The narrow absorption lines are most likely intervening.

*SDSSJ142921.87+540611.2*. This object is classified as an FSRQ by Healey et al. (2007), and Massaro et al. (2009), and listed as a lensed quasar candidate by King et al. (1999). Browne et al. (2003) rejected the lensing hypothesis based upon surface brightness and spectral indices criteria.

*SDSSJ154929.43+023701.1*. This object is classified as an FSRQ (Healey et al. 2007) with high polarization (Scarpa & Falomo 1997). The optical spectrum from SDSS, however, contains strong Mg II  $\lambda$ 2798, H $\beta$ , and even H  $\gamma$  lines. Even some weak forbidden lines are prominent, e.g., the two [Ne V] lines around 3400 Å. This is another case in which a blazar has a regular broad line quasar spectrum.

*SDSSJ161742.53+322234.3*. This is the strong ratio quasar 3C 332. The H $\beta$  line is relatively weak, but the H $\alpha$  line exhibits a very prominent double peak structure with a FWHM of 19,600 km s<sup>-1</sup> measured by Strateva et al. (2006) and 23,200 km s<sup>-1</sup> measured by Wu & Liu (2004). The black hole mass is large,  $\log(M_{\text{BH}}/M_{\odot}) = 9.334$  (Wu & Liu 2004). The H $\alpha$  line also displays long-term profile variability which can be explained by a low, smooth, secular change in disk illumination (Gezari et al. 2007).

*SDSSJ162901.30+400759.9*. This object is classified as a blazar by Massaro et al. (2009), an FSRQ by Falcone et al. (2004),

and a NLS1 galaxy by Bade et al. (1995); Grupe et al. (2004); Komossa et al. (2006). The optical spectrum exhibits strong H $\alpha$ , H $\beta$ , and a complex of low ionization Fe II emission.

*SDSSJ170231.06+324719.6*. This is a typical NLS1 (Grupe et al. 2004; Zhou et al. 2006; Grupe et al. 2010).

*SDSSJ213638.58+004154.1*. This  $z = 1.9414$  FSRQ has a strong radio jet (Liu & Zhang 2002; Healey et al. 2007; Massaro et al. 2009). The UV spectrum contains strong Mg II  $\lambda$ 2798, C IV  $\lambda$ 1549, and C III  $\lambda$ 1908 emission lines.



## REFERENCES

- Abazajian, K., et al. 2005, *AJ*, 129, 1755
- Abdo, A. A., et al. 2010, *ApJ*, 716, 30
- Adelman-McCarthy, J. K., et al. 2007, *ApJS*, 172, 634
- Anderson, S. F., & Margon, B. 1987, *ApJ*, 314, 111
- Anderson, S. F., et al. 2003, *AJ*, 126, 2209
- Arnaud, K. A. 1996, in *Astronomical Society of the Pacific Conference Series*, Vol. 101, *Astronomical Data Analysis Software and Systems V*, ed. G. H. Jacoby & J. Barnes, 17–+
- Arnaud, K. A., et al. 1985, *MNRAS*, 217, 105
- Atlee, D. W., & Mathur, S. 2009, *ApJ*, 703, 1597
- Avni, Y., & Tananbaum, H. 1982, *ApJ*, 262, L17
- . 1986, *ApJ*, 305, 83
- Avni, Y., Worrall, D. M., & Morgan, Jr., W. A. 1995, *ApJ*, 454, 673
- Bade, N., Fink, H. H., Engels, D., Voges, W., Hagen, H., Wisotzki, L., & Reimers, D. 1995, *A&AS*, 110, 469
- Becker, R. H., White, R. L., & Helfand, D. J. 1995, *ApJ*, 450, 559
- Beckmann, V., Engels, D., Bade, N., & Wucknitz, O. 2003, *A&A*, 401, 927
- Blackburn, J. K. 1995, in *Astronomical Society of the Pacific Conference Series*, Vol. 77, *Astronomical Data Analysis Software and Systems IV*, ed. R. A. Shaw, H. E. Payne, & J. J. E. Hayes, 367
- Blandford, R. D., & Rees, M. J. 1978, in *BL Lac Objects*, ed. A. M. Wolfe, 328–341
- Boggess, A., et al. 1978, *Nature*, 275, 372
- Brandt, W. N., Laor, A., & Wills, B. J. 2000, *ApJ*, 528, 637
- Brinkmann, W., Laurent-Muehleisen, S. A., Voges, W., Siebert, J., Becker, R. H., Brotherton, M. S., White, R. L., & Gregg, M. D. 2000, *A&A*, 356, 445
- Browne, I. W. A., et al. 2003, *MNRAS*, 341, 13
- Buckley, J., & James, I. 1979, *Biometrika*, 1, 66
- Burrows, D. N., et al. 2005, *Space Sci. Rev.*, 120, 165
- Cash, W. 1979, *ApJ*, 228, 939
- Cheung, C. C. 2007, *AJ*, 133, 2097
- Cohen, M., Wheaton, W. A., & Megeath, S. T. 2003, *AJ*, 126, 1090
- Collinge, M. J., et al. 2005, *AJ*, 129, 2542
- Condon, J. J., Cotton, W. D., Greisen, E. W., Yin, Q. F., Perley, R. A., Taylor, G. B., & Broderick, J. J. 1998, *AJ*, 115, 1693
- Congdon, A. B., Keeton, C. R., & Nordgren, C. E. 2010, *ApJ*, 709, 552
- della Ceca, R., Lamorani, G., Maccacaro, T., Wolter, A., Griffiths, R., Stocke, J. T., & Setti, G. 1994, *ApJ*, 430, 533
- Dempster, A. P., Laird, N. M., & Rubin, D. B. 1977, *Royal Stat. Soc. B*, 39, 1
- Dong, X., Zhou, H., Wang, T., Wang, J., Li, C., & Zhou, Y. 2005, *ApJ*, 620, 629
- Elvis, M., et al. 1994, *ApJS*, 95, 1
- Elvis, M., s. 2012
- Falcone, A. D., et al. 2004, *ApJ*, 613, 710
- Fitzpatrick, E. L. 1999, *PASP*, 111, 63

- Fukugita, M., Ichikawa, T., Gunn, J. E., Doi, M., Shimasaku, K., & Schneider, D. P. 1996, *AJ*, 111, 1748
- Gaskell, C. M., & Klimek, E. S. 2003, *Astronomical and Astrophysical Transactions*, 22, 661
- Gehrels, N., et al. 2004, *ApJ*, 611, 1005
- George, I. M., Turner, T. J., Yaqoob, T., Netzer, H., Laor, A., Mushotzky, R. F., Nandra, K., & Takahashi, T. 2000, *ApJ*, 531, 52
- Gezari, S., Halpern, J. P., & Eracleous, M. 2007, *ApJS*, 169, 167
- Gibson, R. R., et al. 2009, *ApJ*, 692, 758
- Gierliński, M., & Done, C. 2004, *MNRAS*, 349, L7
- Griffith, M. R., Wright, A. E., Burke, B. F., & Ekers, R. D. 1995, *ApJS*, 97, 347
- Grupe, D., Beuermann, K., Mannheim, K., & Thomas, H.-C. 1999, *A&A*, 350, 805
- Grupe, D., Komossa, S., Gallo, L. C., Fabian, A. C., Larsson, J., Pradhan, A. K., Xu, D., & Miniutti, G. 2008, *ApJ*, 681, 982
- Grupe, D., Komossa, S., Leighly, K. M., & Page, K. L. 2010, *ApJS*, 187, 64
- Grupe, D., Wills, B. J., Leighly, K. M., & Meusinger, H. 2004, *AJ*, 127, 156
- Hall, P. B., Gallagher, S. C., Richards, G. T., Alexander, D. M., Anderson, S. F., Bauer, F., Brandt, W. N., & Schneider, D. P. 2006, *AJ*, 132, 1977
- Hao, L., et al. 2005, *AJ*, 129, 1795
- Hartmann, D., & Burton, W. B. 1997, *Atlas of Galactic Neutral Hydrogen*, ed. Hartmann, D. & Burton, W. B.
- Healey, S. E., Romani, R. W., Taylor, G. B., Sadler, E. M., Ricci, R., Murphy, T., Ulvestad, J. S., & Winn, J. N. 2007, *ApJS*, 171, 61
- Hopkins, P. F., et al. 2004, *AJ*, 128, 1112
- Inada, N., et al. 2010, *AJ*, 140, 403
- Jolley, E. J. D., Kuncic, Z., Bicknell, G. V., & Wagner, S. 2009, *MNRAS*, 400, 1521
- Just, D. W., Brandt, W. N., Shemmer, O., Steffen, A. T., Schneider, D. P., Chartas, G., & Garmire, G. P. 2007, *ApJ*, 665, 1004
- Kalberla, P. M. W., Burton, W. B., Hartmann, D., Arnal, E. M., Bajaja, E., Morras, R., & Pöppel, W. G. L. 2005, *A&A*, 440, 775
- Kellermann, K. I., Sramek, R., Schmidt, M., Shaffer, D. B., & Green, R. 1989, *AJ*, 98, 1195
- Kelly, B. C., Bechtold, J., Siemiginowska, A., Aldcroft, T., & Sobolewska, M. 2007, *ApJ*, 657, 116
- King, L. J., Browne, I. W. A., Marlow, D. R., Patnaik, A. R., & Wilkinson, P. N. 1999, *MNRAS*, 307, 225
- Kollgaard, R. I. 1994, *Vistas in Astronomy*, 38, 29
- Komossa, S., Voges, W., Xu, D., Mathur, S., Adorf, H., Lemson, G., Duschl, W. J., & Grupe, D. 2006, *AJ*, 132, 531
- Kondo, Y., Boggess, A., & Maran, S. P. 1989, *ARA&A*, 27, 397
- Kovalev, Y. Y., Kovalev, Y. A., Nizhelsky, N. A., & Bogdantsov, A. B. 2002, *PASA*, 19, 83
- Kraft, R. P., Burrows, D. N., & Nousek, J. A. 1991, *ApJ*, 374, 344
- Laor, A., Fiore, F., Elvis, M., Wilkes, B. J., & McDowell, J. C. 1997, *ApJ*, 477, 93

- Lavalley, M., Isobe, T., & Feigelson, E. 1992, in *Astronomical Society of the Pacific Conference Series*, Vol. 25, *Astronomical Data Analysis Software and Systems I*, ed. D. M. Worrall, C. Biemesderfer, & J. Barnes, 245–+
- Lehmer, B. D., et al. 2007, *ApJ*, 657, 681
- Liu, F. K., & Zhang, Y. H. 2002, *A&A*, 381, 757
- Longair, M. S. 1992, *High energy astrophysics. Vol.1: Particles, photons and their detection*, ed. Longair, M. S.
- Lu, Y., Wang, T., Zhou, H., & Wu, J. 2007, *AJ*, 133, 1615
- Lupton, R. H., Gunn, J. E., & Szalay, A. S. 1999, *AJ*, 118, 1406
- Marshall, H. L., Huchra, J. P., Tananbaum, H., Avni, Y., Braccisi, A., Zitelli, V., & Zamorani, G. 1984, *ApJ*, 283, 50
- Massaro, E., Giommi, P., Leto, C., Marchegiani, P., Maselli, A., Perri, M., Piranomonte, S., & Scavi, S. 2009, *A&A*, 495, 691
- Mathews, W. G., & Ferland, G. J. 1987, *ApJ*, 323, 456
- Mathur, S., Elvis, M., & Wilkes, B. 1995, *ApJ*, 452, 230
- Matthews, T. A., & Sandage, A. R. 1963, *ApJ*, 138, 30
- McLure, R. J., & Dunlop, J. S. 2004, *MNRAS*, 352, 1390
- McLure, R. J., & Jarvis, M. J. 2002, *MNRAS*, 337, 109
- Meusinger, H., Hinze, A., & de Hoon, A. 2011, *A&A*, 525, A37+
- Miller, B. P., Brandt, W. N., Gibson, R. R., Garmire, G. P., & Shemmer, O. 2009, *ApJ*, 702, 911
- Mukai, K. 1993, *Legacy*, vol. 3, p.21-31, 3, 21
- Nandra, K., & Pounds, K. A. 1994, *MNRAS*, 268, 405
- Padovani, P., Giommi, P., Landt, H., & Perlman, E. S. 2007, *ApJ*, 662, 182
- Page, K. L., Reeves, J. N., O’Brien, P. T., & Turner, M. J. L. 2005, *MNRAS*, 364, 195
- Page, K. L., Reeves, J. N., O’Brien, P. T., Turner, M. J. L., & Worrall, D. M. 2004, *MNRAS*, 353, 133
- Page, K. L., Turner, M. J. L., Reeves, J. N., O’Brien, P. T., & Sembay, S. 2003, *MNRAS*, 338, 1004
- Park, S. Q., et al. 2010, *ApJ*, 717, 1181
- Peng, C. Y., Ho, L. C., Impey, C. D., & Rix, H. 2002, *AJ*, 124, 266
- . 2010, *AJ*, 139, 2097
- Peterson, B. M., et al. 2004, *ApJ*, 613, 682
- Pickering, T. E., Impey, C. D., & Foltz, C. B. 1994, *AJ*, 108, 1542
- Plotkin, R. M., Anderson, S. F., Hall, P. B., Margon, B., Voges, W., Schneider, D. P., Stinson, G., & York, D. G. 2008, *AJ*, 135, 2453
- Pogson, N. 1857, *MNRAS*, 18, 47
- Poole, T. S., et al. 2008, *MNRAS*, 383, 627
- Rani, B., Gupta, A. C., Joshi, U. C., Ganesh, S., & Wiita, P. J. 2010, *ApJ*, 719, L153
- Rauch, M. 1998, *ARA&A*, 36, 267
- Richards, G. T. 2001, *ApJS*, 133, 53
- Richards, G. T., et al. 2003, *AJ*, 126, 1131
- . 2006, *ApJS*, 166, 470
- Rieger, F. M., & Aharonian, F. A. 2008, *A&A*, 479, L5

- Risaliti, G., & Elvis, M. 2005, *ApJ*, 629, L17
- Roming, P. W. A., et al. 2005, *Space Sci. Rev.*, 120, 95
- . 2009, *ApJ*, 690, 163
- Sakata, Y., et al. 2010, *ApJ*, 711, 461
- Sambruna, R. M., et al. 2006, *ApJ*, 646, 23
- Scarpa, R., & Falomo, R. 1997, *A&A*, 325, 109
- Schlegel, D. J., Finkbeiner, D. P., & Davis, M. 1998, *ApJ*, 500, 525
- Schneider, D. P., et al. 2005, *AJ*, 130, 367
- . 2007, *AJ*, 134, 102
- Shang, Z., et al. 2005, *ApJ*, 619, 41
- Shemmer, O., Brandt, W. N., Netzer, H., Maiolino, R., & Kaspi, S. 2006, *ApJ*, 646, L29
- . 2008, *ApJ*, 682, 81
- Shemmer, O., Brandt, W. N., Vignali, C., Schneider, D. P., Fan, X., Richards, G. T., & Strauss, M. A. 2005, *ApJ*, 630, 729
- Shen, J., Vanden Berk, D. E., Schneider, D. P., & Hall, P. B. 2008a, *AJ*, 135, 928
- Shen, Y., Greene, J. E., Strauss, M. A., Richards, G. T., & Schneider, D. P. 2008b, *ApJ*, 680, 169
- Shields, G. A. 1978, *Nature*, 272, 706
- Skrutskie, M. F., et al. 2006, *AJ*, 131, 1163
- Smith, H. J., & Hoffleit, D. 1963, *Nature*, 198, 650
- Steffen, A. T., Strateva, I., Brandt, W. N., Alexander, D. M., Koekemoer, A. M., Lehmer, B. D., Schneider, D. P., & Vignali, C. 2006, *AJ*, 131, 2826
- Stoeckle, J. T., Morris, S. L., Weymann, R. J., & Foltz, C. B. 1992, *ApJ*, 396, 487
- Strateva, I. V., Brandt, W. N., Eracleous, M., Schneider, D. P., & Chartas, G. 2006, *ApJ*, 651, 749
- Strateva, I. V., Brandt, W. N., Schneider, D. P., Vanden Berk, D. G., & Vignali, C. 2005, *AJ*, 130, 387
- Tananbaum, H., Avni, Y., Green, R. F., Schmidt, M., & Zamorani, G. 1986, *ApJ*, 305, 57
- Tananbaum, H., et al. 1979, *ApJ*, 234, L9
- Telfer, R. C., Zheng, W., Kriss, G. A., & Davidsen, A. F. 2002, *ApJ*, 565, 773
- Trump, J. R., et al. 2006, *ApJS*, 165, 1
- Tueller, J., Mushotzky, R. F., Barthelmy, S., Cannizzo, J. K., Gehrels, N., Markwardt, C. B., Skinner, G. K., & Winter, L. M. 2008, *ApJ*, 681, 113
- Turner, T. J., Miller, L., George, I. M., & Reeves, J. N. 2006, *A&A*, 445, 59
- Turner, T. J., Miller, L., Reeves, J. N., & Kraemer, S. B. 2007, *A&A*, 475, 121
- Turner, T. J., & Pounds, K. A. 1989, *MNRAS*, 240, 833
- Ueda, Y., et al. 2007, *ApJ*, 664, L79
- Urry, C. M., & Padovani, P. 1995, *PASP*, 107, 803
- Vanden Berk, D. E., et al. 2001, *AJ*, 122, 549
- . 2004, *ApJ*, 601, 692
- Vasudevan, R. V., & Fabian, A. C. 2009, *MNRAS*, 392, 1124
- Véron-Cetty, M., Joly, M., & Véron, P. 2004, *A&A*, 417, 515
- Vestergaard, M., & Peterson, B. M. 2006, *ApJ*, 641, 689

- Vestergaard, M., & Wilkes, B. J. 2001, *ApJS*, 134, 1
- Vignali, C., Brandt, W. N., & Schneider, D. P. 2003, *AJ*, 125, 433
- Vignali, C., Brandt, W. N., Schneider, D. P., & Kaspi, S. 2005, *AJ*, 129, 2519
- Walter, R., & Fink, H. H. 1993, *A&A*, 274, 105
- Wang, T., Dong, X., Zhang, X., Zhou, H., Wang, J., & Lu, Y. 2005, *ApJ*, 625, L35
- Watanabe, S., et al. 2009, *ApJ*, 694, 294
- White, R. L., Becker, R. H., Helfand, D. J., & Gregg, M. D. 1997, *ApJ*, 475, 479
- Wilhite, B. C., Vanden Berk, D. E., Brunner, R. J., & Brinkmann, J. V. 2006, *ApJ*, 641, 78
- Wilhite, B. C., Vanden Berk, D. E., Kron, R. G., Schneider, D. P., Pereyra, N., Brunner, R. J., Richards, G. T., & Brinkmann, J. V. 2005, *ApJ*, 633, 638
- Wilkes, B. J., Kuraszkiewicz, J., Green, P. J., Mathur, S., & McDowell, J. C. 1999, *ApJ*, 513, 76
- Wilkes, B. J., Tananbaum, H., Worrall, D. M., Avni, Y., Oey, M. S., & Flanagan, J. 1994, *ApJS*, 92, 53
- Williams, L. L. R., Foley, P., Farnsworth, D., & Belter, J. 2008, *ApJ*, 685, 725
- Winter, L. M., Mushotzky, R. F., Reynolds, C. S., & Tueller, J. 2009, *ApJ*, 690, 1322
- Wolf, C., Wisotzki, L., Borch, A., Dye, S., Kleinheinrich, M., & Meisenheimer, K. 2003, *A&A*, 408, 499
- Wolf, C., et al. 2004, *A&A*, 421, 913
- Worrall, D. M., Tananbaum, H., Giommi, P., & Zamorani, G. 1987, *ApJ*, 313, 596
- Wu, J., Vanden Berk, D. E., Brandt, W. N., Schneider, D. P., Gibson, R. R., & Wu, J. 2009, *ApJ*, 702, 767
- Wu, X., & Liu, F. K. 2004, *ApJ*, 614, 91
- York, D. G., et al. 2000, *AJ*, 120, 1579
- Young, M., Elvis, M., & Risaliti, G. 2009, *ApJS*, 183, 17
- Zheng, W., Kriss, G. A., Telfer, R. C., Grimes, J. P., & Davidsen, A. F. 1997, *ApJ*, 475, 469
- Zhou, H., Wang, T., Yuan, W., Lu, H., Dong, X., Wang, J., & Lu, Y. 2006, *ApJS*, 166, 128

---

This 2-column preprint was prepared with the AAS L<sup>A</sup>T<sub>E</sub>X macros v5.2.

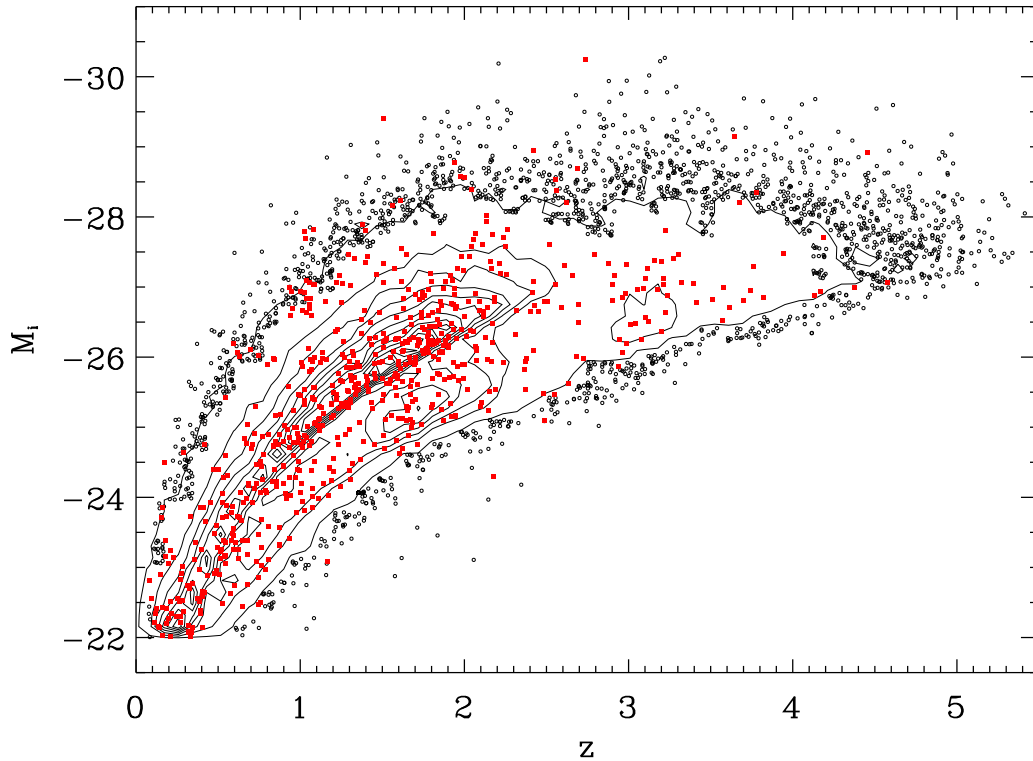


Fig. 1.— Distribution of our sample in the redshift vs. SDSS  $i$  band absolute magnitude diagram. The SDSS DR5 quasar catalog objects are represented by open circles. Their distribution is represented by a set of linear contours when the density of open circles in this two-dimensional space exceeds a certain threshold and the plot symbols begin to overlap. Objects in the *Swift* quasar catalog are represented by red filled squares. The lower luminosity limit occurs because the SDSS DR5 quasar catalog includes only quasars more luminous than  $M_i = 22.0$ .

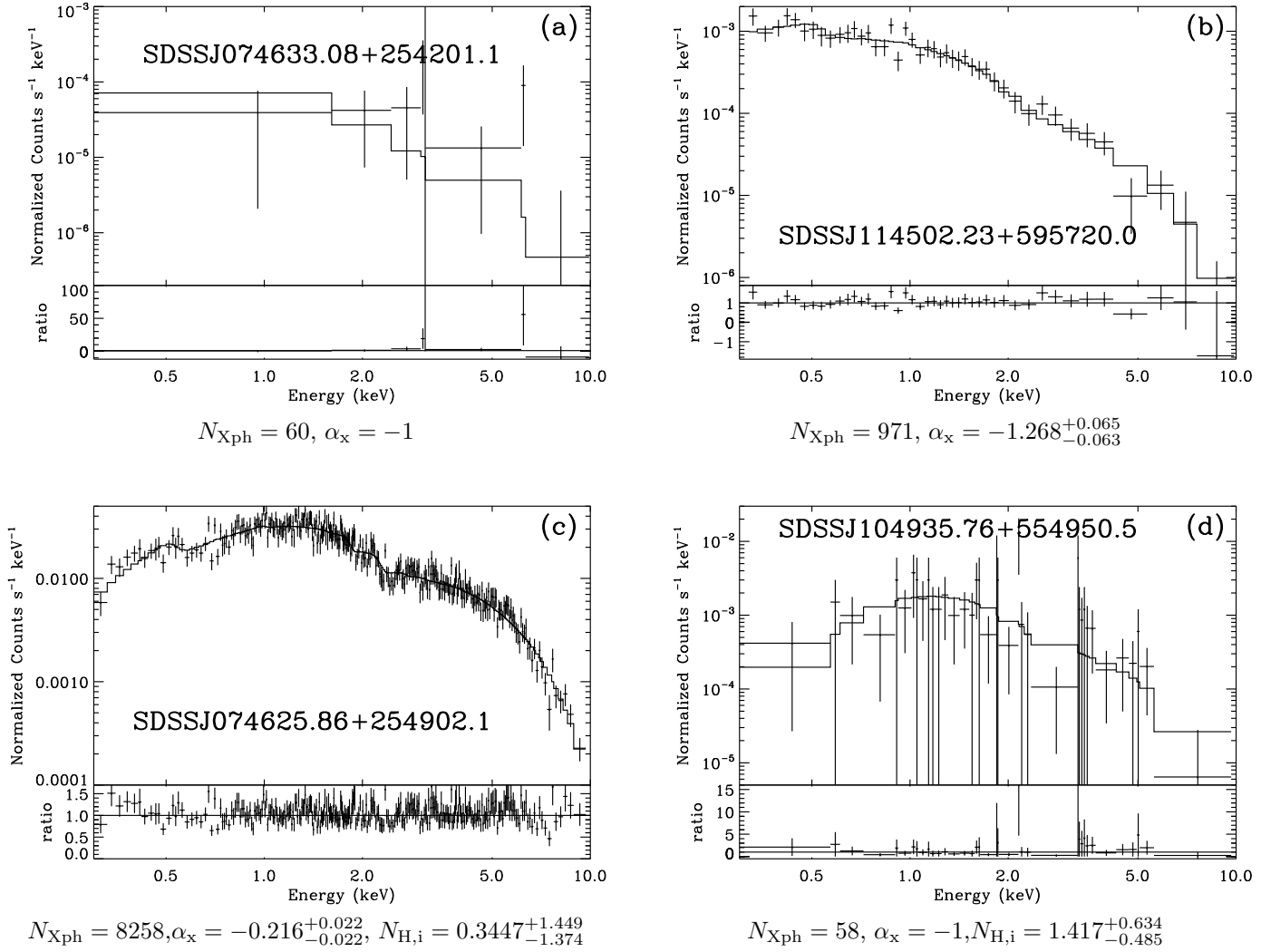


Fig. 2.— Four examples of fits to the observed XRT spectra. Intrinsic column densities ( $N_{\text{H},i}$ ) are in units of  $10^{22} \text{ cm}^{-2}$ . Spectra shown in (b) and (c) are binned as listed in Table 1. Spectra shown in (a) and (d) are *rebinned* using the *XSPEC* command `setplot rebin` (see Section 3.2).

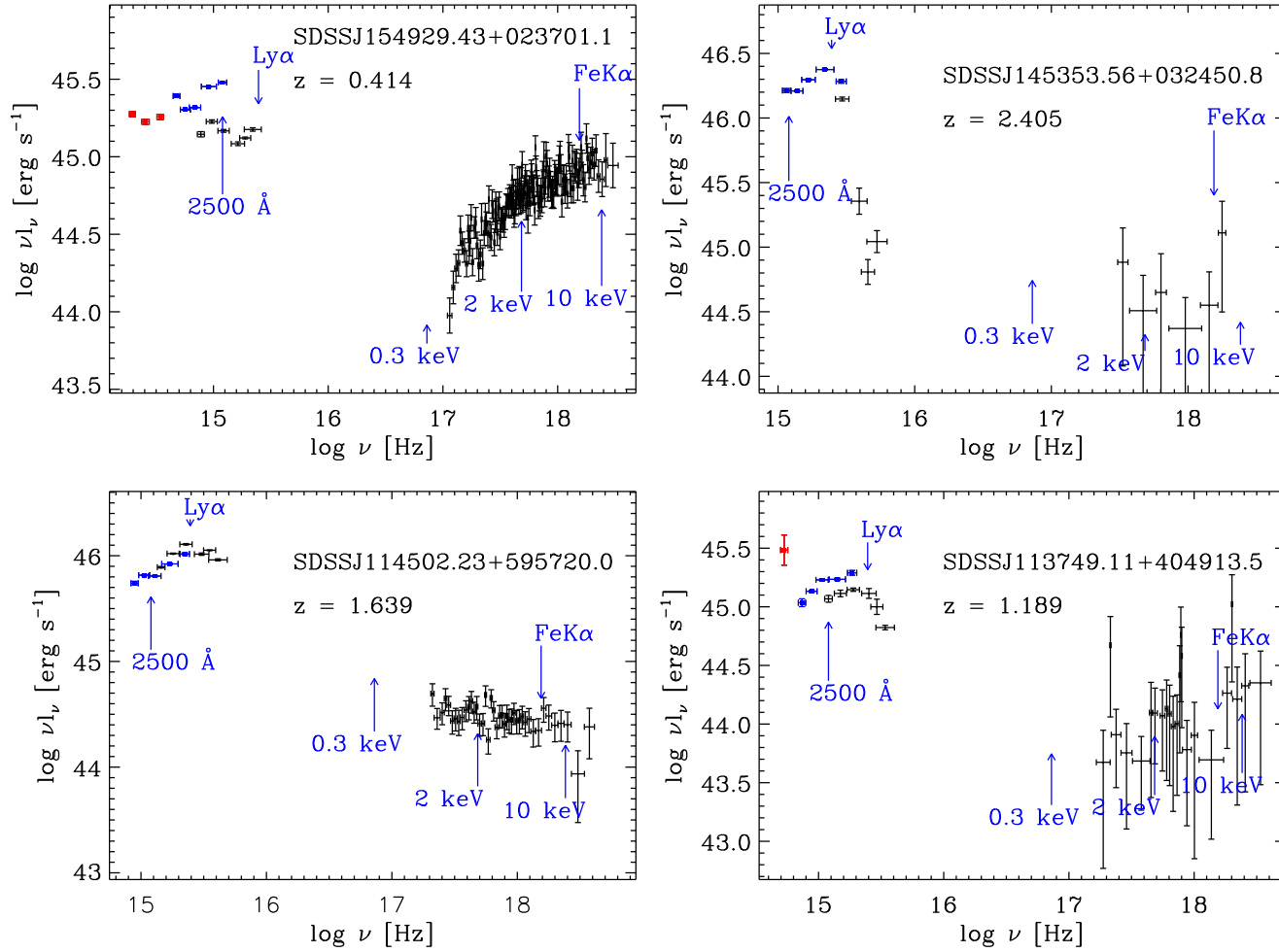


Fig. 3.— Examples of initial SEDs, showing data from *Swift* UVOT and XRT (black), SDSS (blue) and 2MASS (red). There are clear flux offsets between SDSS and UVOT measurements.



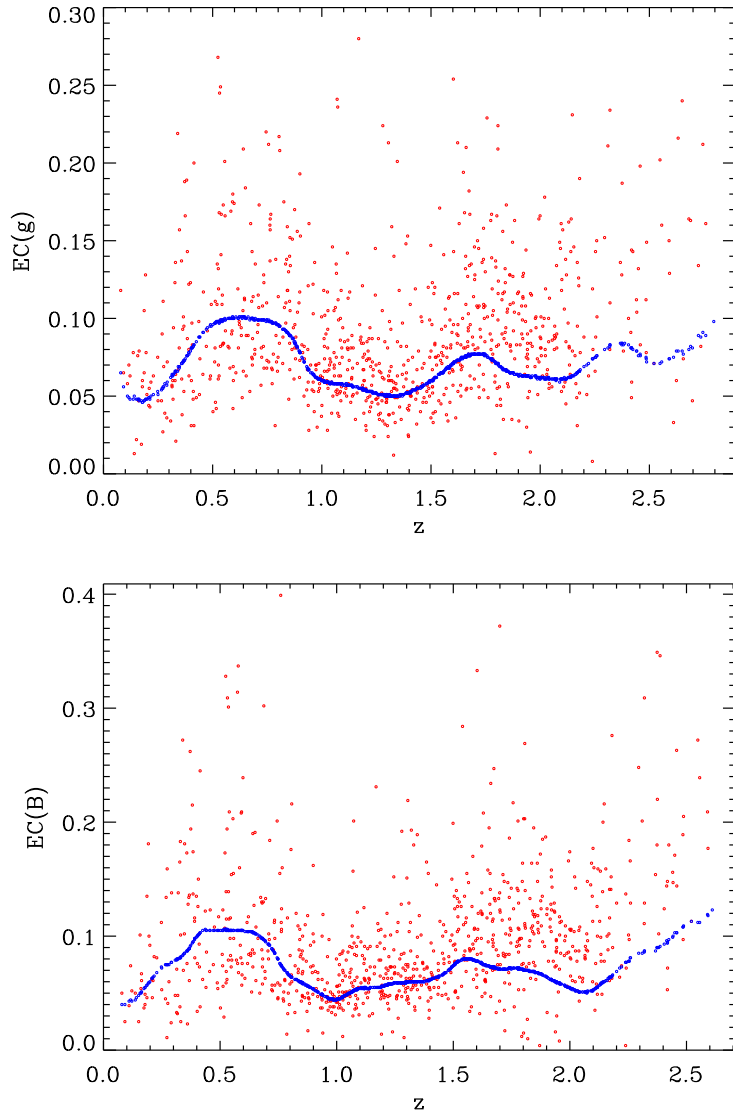


Fig. 4.— Emission line corrections (EC) of the SDSS  $g$  band (*Upper* panel) and the UVOT B band (*lower* panel) as a function of redshift for different filters. Red circles are EC performed on real spectra. Blue circles are EC performed on the composite spectrum by Vanden Berk et al. (2001) shifted to the real spectrum redshift. The EC represented by blue circles varies with redshift as emission lines are shifted within the coverage of a filter. These plots indicate that the ECs based on real spectra are generally in agreement with ECs based on the composite spectrum.

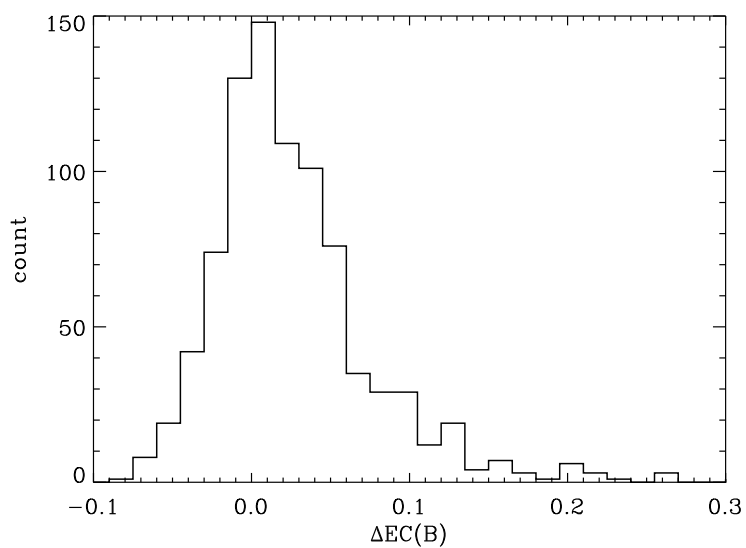
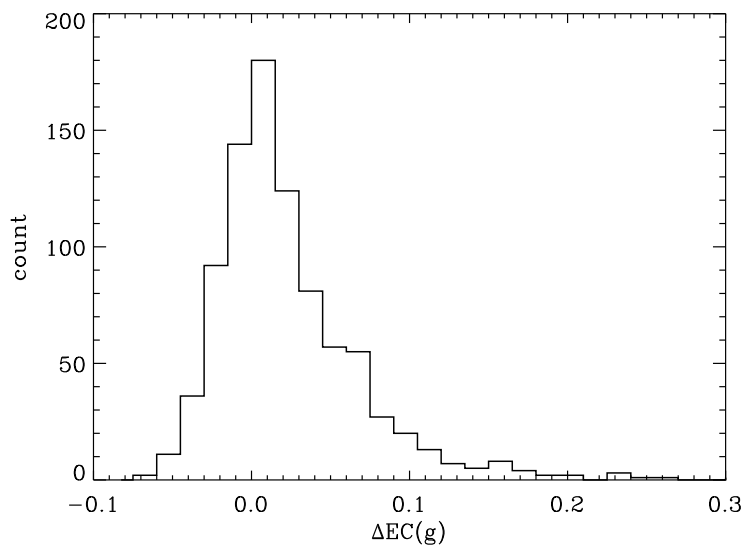


Fig. 5.— Distributions of emission line correction differences  $\Delta EC = EC_{\text{real}} - EC_{\text{composite}}$  in the SDSS  $g$  band and the UVOT B band based on the results shown in Figure 4. These figures illustrate that we can in general obtain consistent ECs based on real and composite spectra at different bands. The dispersion of their difference is typically 0.05.

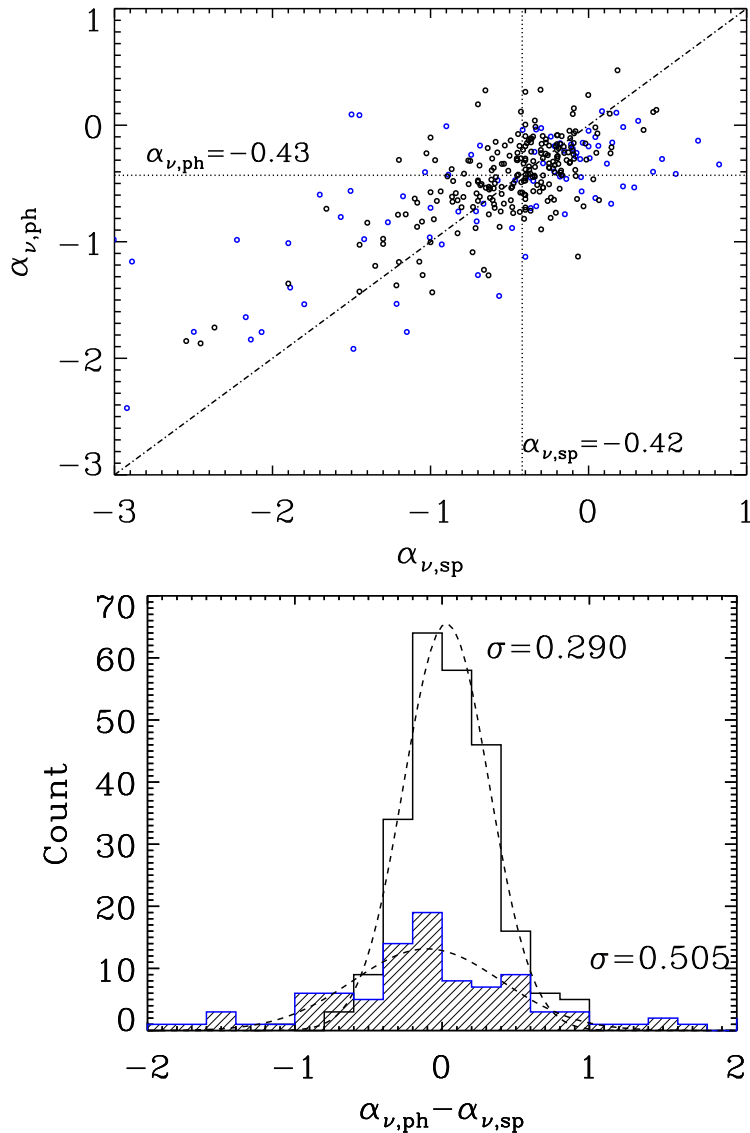


Fig. 6.— *Upper:* photometric UV slope  $\alpha_{\nu,\text{ph}}$  vs. spectroscopic UV slope  $\alpha_{\nu,\text{sp}}$ . Low-redshift objects ( $z < 0.8$ ) are in blue and objects at higher redshifts ( $z > 0.8$ ) are in black. The dash dotted line is  $\alpha_{\nu,\text{ph}} = \alpha_{\nu,\text{sp}}$ . The dotted lines represent the median values of  $\alpha_{\nu,\text{ph}} = -0.43$  and  $\alpha_{\nu,\text{sp}} = -0.42$ , respectively. *Lower:* Distribution of differences between  $\alpha_{\nu,\text{ph}}$  and  $\alpha_{\nu,\text{sp}}$  for low-redshift ( $z < 0.8$ , in blue) and high-redshift ( $z > 0.8$ , in black) objects. We also fit these two histograms with Gaussian profiles. The low redshift sample has a dispersion ( $\sigma \approx 0.5$ ) much larger than the higher redshift sample dispersion ( $\sigma \approx 0.3$ ).

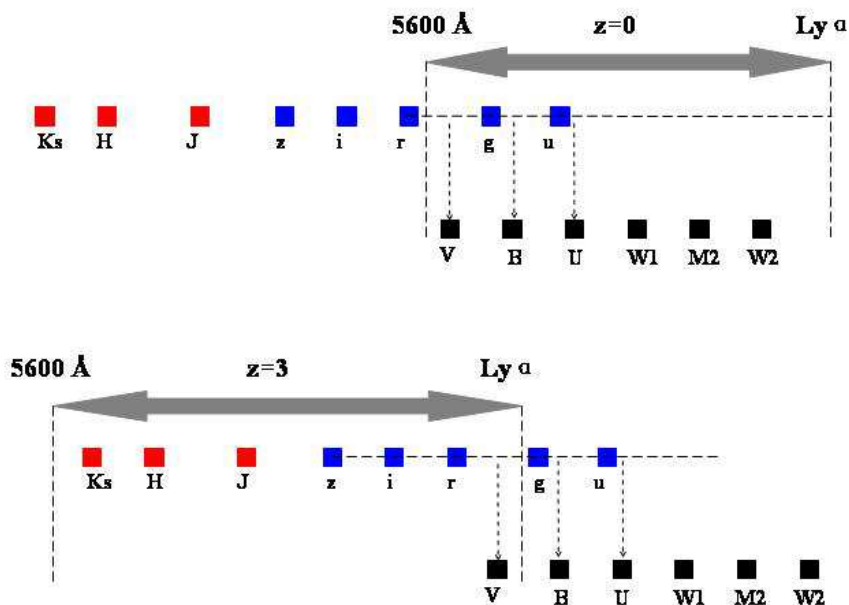


Fig. 7.— Illustration of the photometric shift strategy at  $z = 0$  and  $z = 3$ . In either case, SDSS photometry is interpolated or extrapolated to the wavelengths of the UVOT filters. The SDSS and 2MASS data are then shifted by the difference between real and interpolated luminosities. Because the 2MASS do not overlap with the UVOT wavebands, we shift the 2MASS photometry with the same value as SDSS photometry (see Section 3.4).

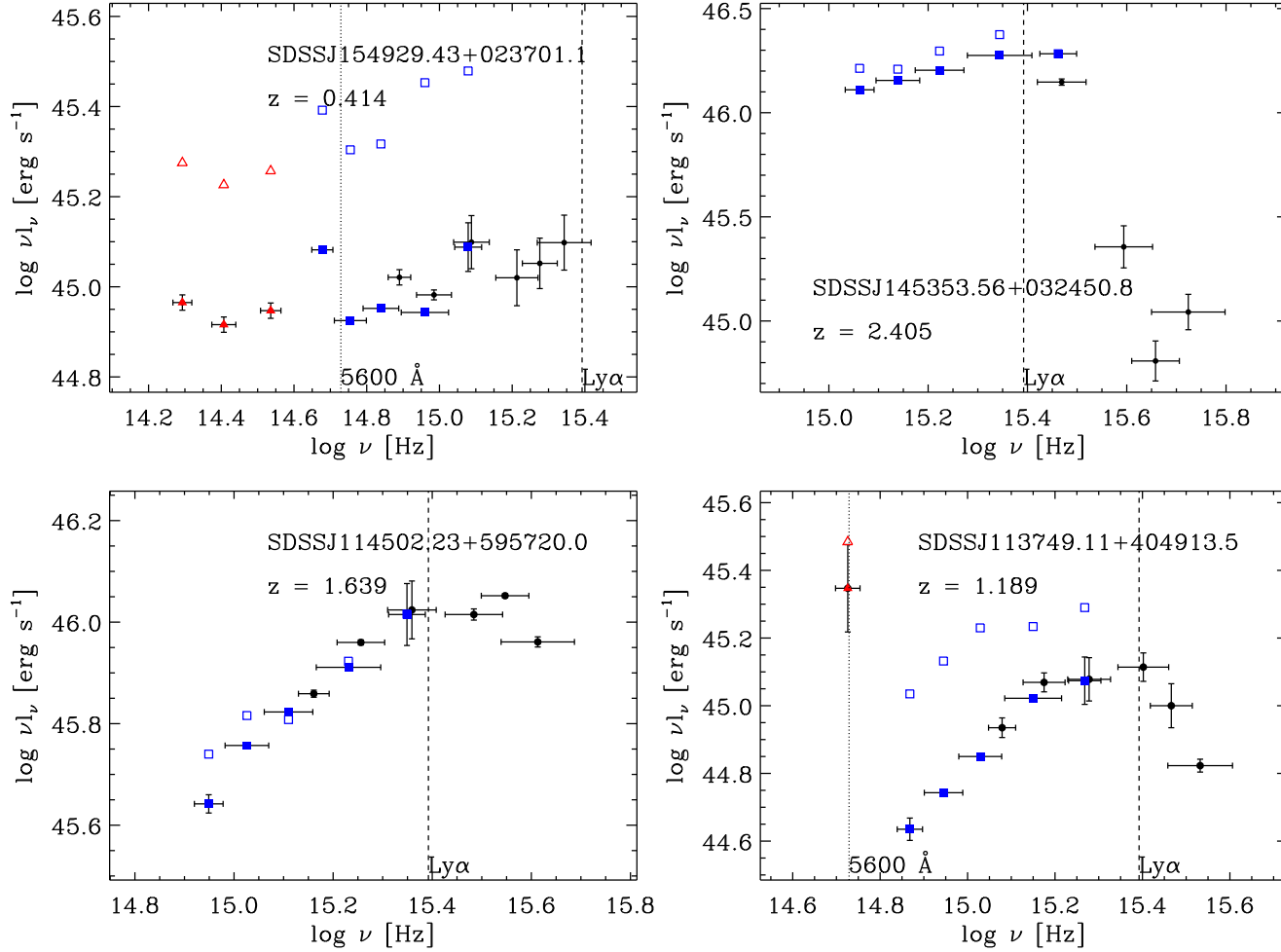


Fig. 8.— Emission line corrected and photometric shifted SEDs for four quasars. The X-ray data points ( $\log \nu > 17$ ) are not plotted because the corrections are only applied to UV/optical data. In the band with  $\log \nu(5600 \text{ \AA}) < \log \nu < \log \nu(\text{Ly } \alpha)$ , data points from UVOT are represented by black dots with error bars; SDSS data points are represented by blue squares and 2MASS data points are represented by red triangles. Open shapes represent photometry before correction, while filled shapes show photometry after correction. Photometric points outside the  $\text{Ly}\alpha$ - $5600 \text{ \AA}$  region are not corrected for line emission.

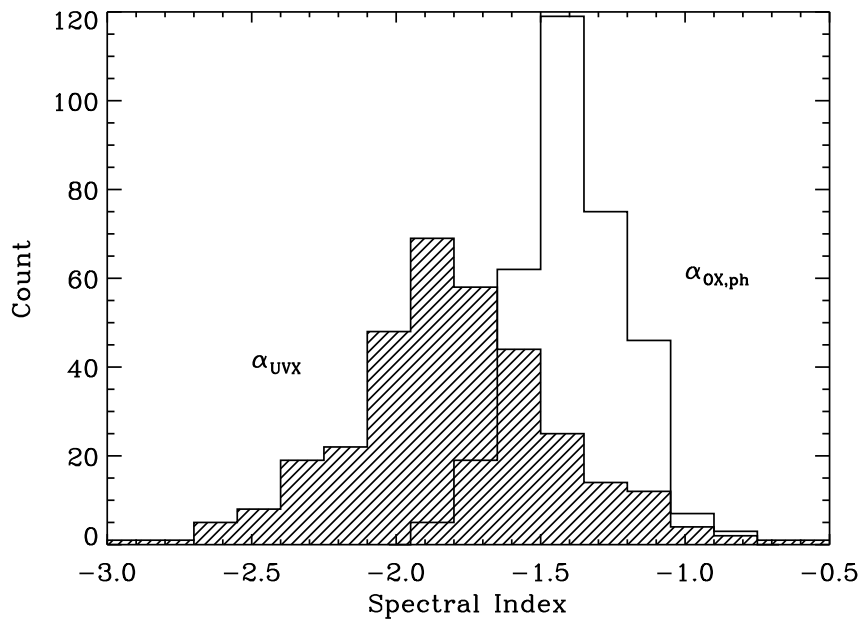


Fig. 9.— Distribution of  $\alpha_{UVX}$  (shaded) and  $\alpha_{ox}$  (unshaded) using photometric data. The median value of  $\alpha_{UVX}$  is considerably steeper than that for  $\alpha_{ox}$  (-1.8 vs. -1.39).

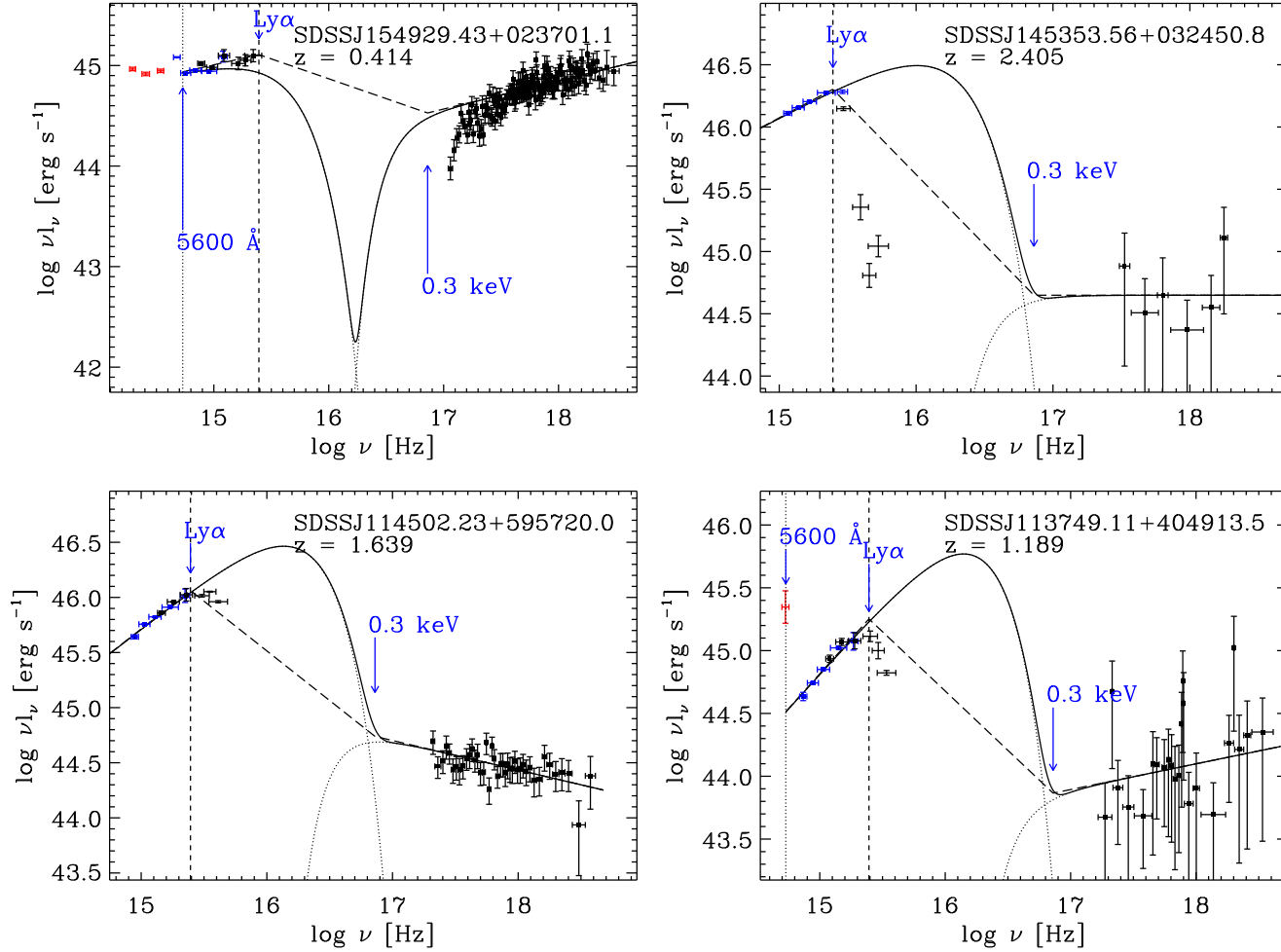


Fig. 10.— Examples of SED fits with the EXP (solid curves) and TPL (dashed lines) models. The UV/optical fitting region is bounded with a vertical dotted line at 5600 Å and a vertical dashed line at Ly $\alpha$ . UV/optical data points outside this region are not used for SED fitting. *Swift* UVOT data are plotted in black; SDSS data are plotted in blue; 2MASS data are plotted in red. Dotted curves are UV and X-ray components for the EXP model. SDSSJ154929.43+023701.1 is a case with strong UV and X-ray absorption, in which the EXP model no longer provides an upper limit to BBB emission.

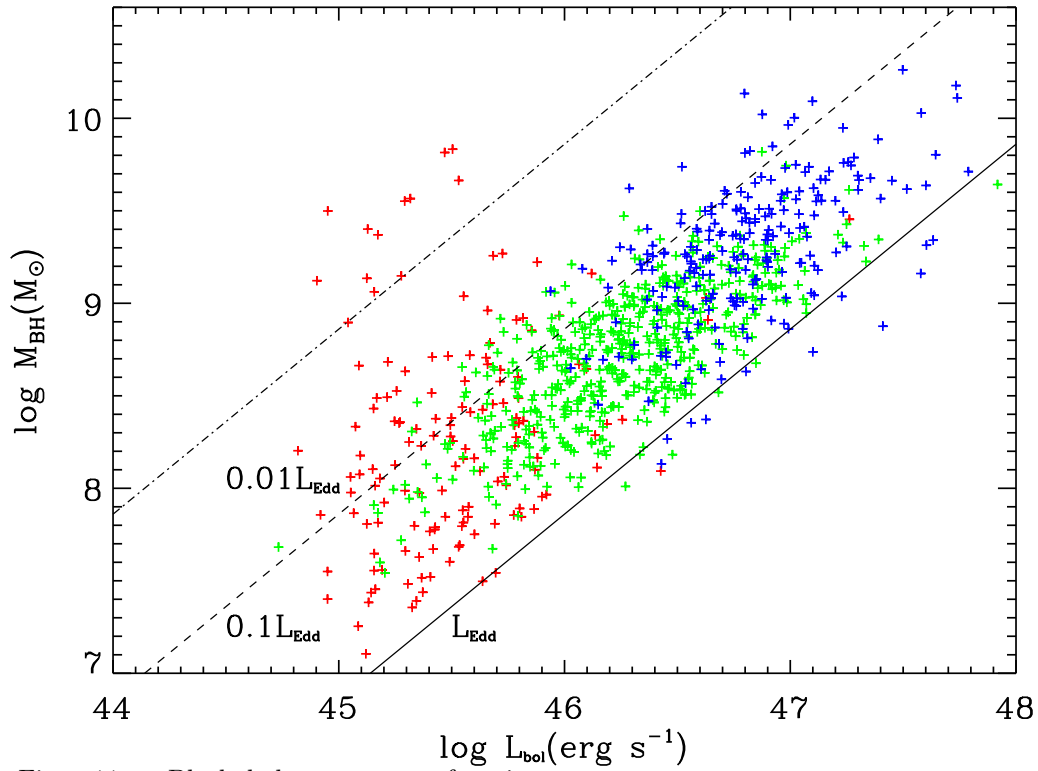


Fig. 11.— Black hole mass as a function of bolometric luminosity for 923 quasars in our catalog. Quasars are color-coded based on their redshift ranges following the same convention as Shen et al. (2008b): red for  $z < 0.7$ , green for  $0.7 < z < 1.9$ , and blue for  $z > 1.9$ . We also plot solid, dashed and dash-dot lines when the Eddington ratio is 1, 0.1 and 0.01, respectively.



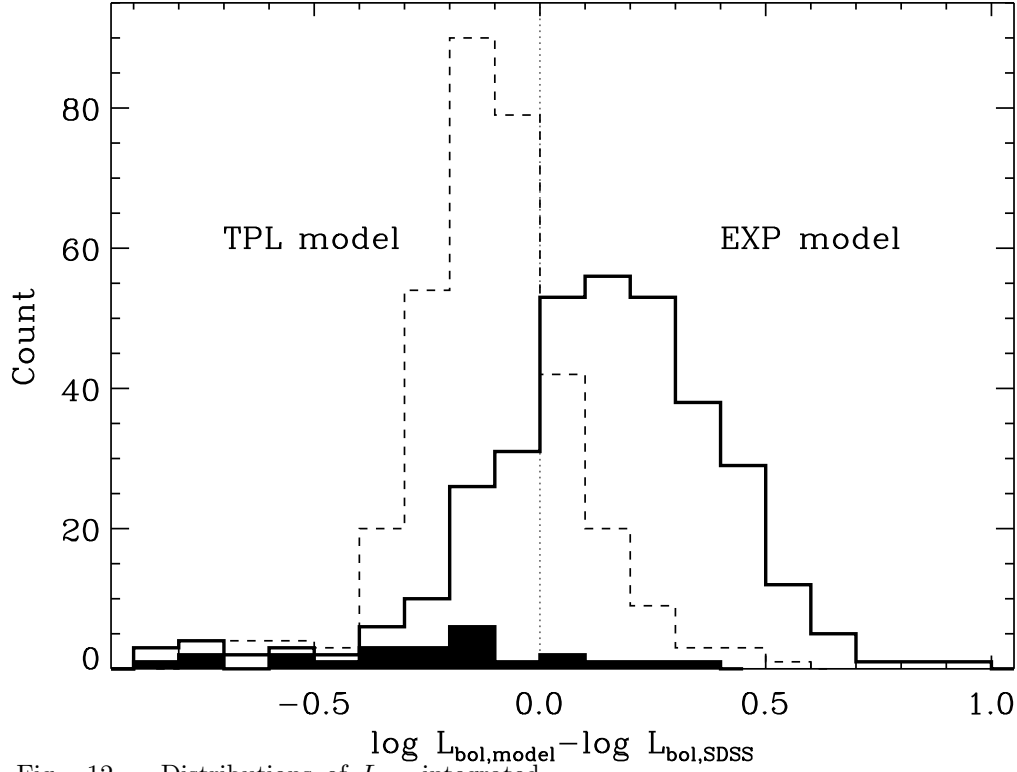


Fig. 12.— Distributions of  $L_{\text{bol}}$  integrated from the EXP (thick solid line) and TPL (thin dashed line) models with respect to  $L_{\text{bol}}$  calculated using the BC correction. The black shaded region under the EXP model histogram represents objects we flagged as “red” which suffer from strong intrinsic absorption (see the “Reddened quasars” in Section 5.1).

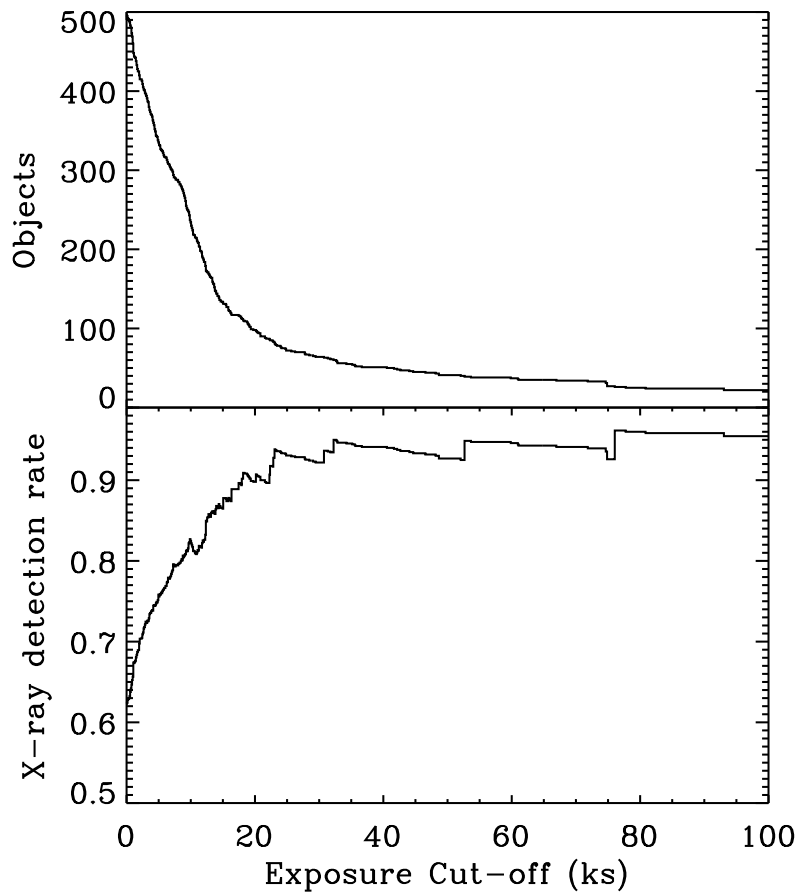


Fig. 13.— The clean catalog sample size (*Upper panel*) and X-ray detection rate (*Lower panel*) as a function of XRT exposure cut-off in kilo-seconds.

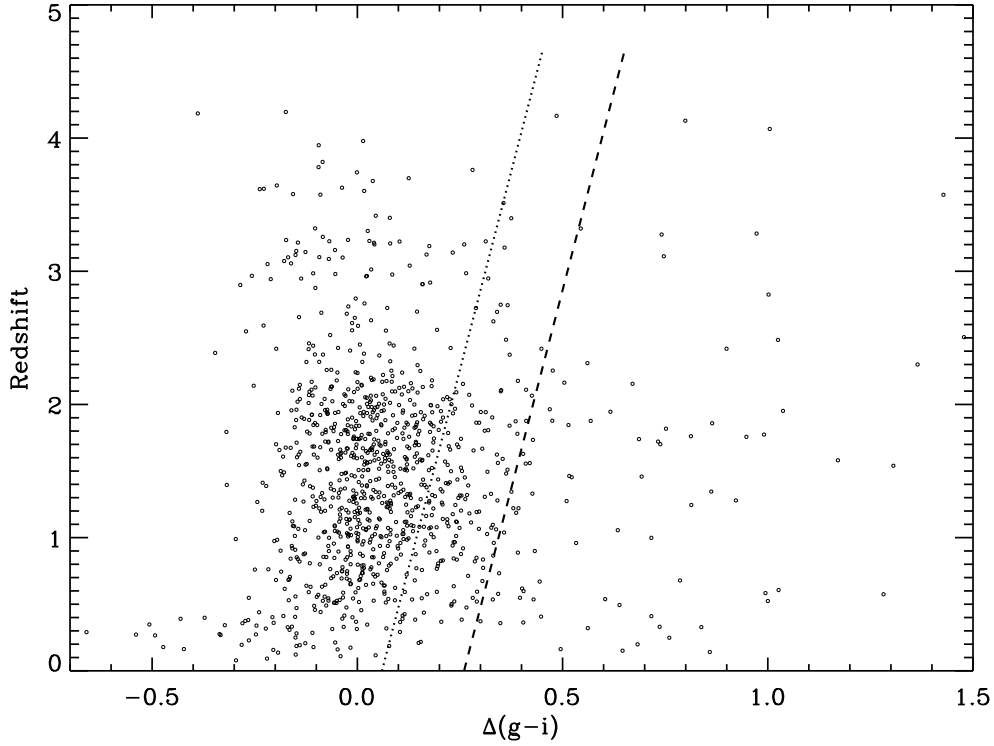


Fig. 14.— The relative color  $\Delta(g-i)$  vs. redshift diagram of all the objects in the raw catalog. The dotted line shows the effect of SMC-type reddening as a function of redshift with  $E(B-V) = 0.04$  (see Richards et al. 2003 for the choice of 0.04 as the value of  $E(B-V)$ ). The dashed line is the dotted line shifted by 0.2 to match the dust-reddening quasar definition of Richards et al. (2003). Quasars to the right of the dashed line are considered to be dust-reddened.

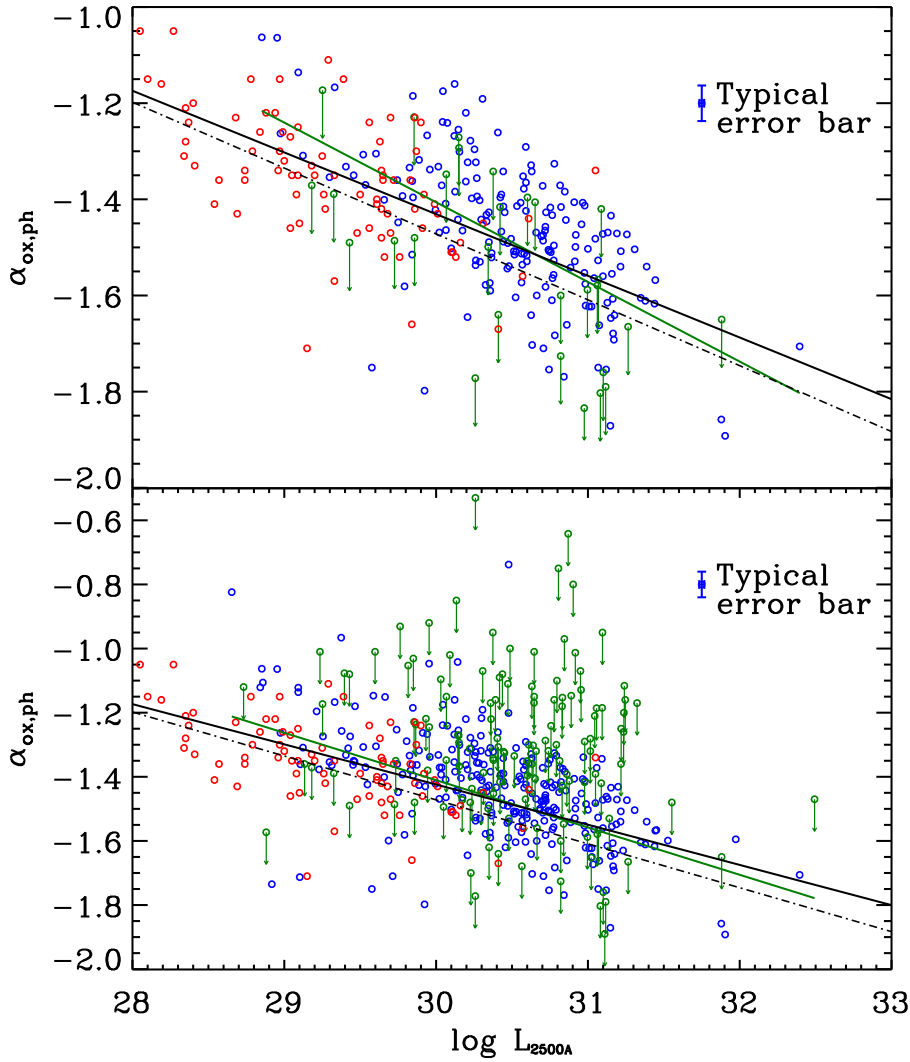


Fig. 15.— The  $\alpha_{\text{ox}}-L_{2500 \text{ \AA}}$  relation for the clean sample with a 10 ks XRT exposure cutoff (*Upper* panel) and the total clean sample (*Lower* panel), including the large clean catalog sample (green+blue, blue points are X-ray detected), and the G10 sample (red). Blue points are X-ray detected, while green points with arrows are upper limits of undetected objects. The solid black line is the best linear fit to the combined sample using the EM method and the solid green line is the best linear fit to the cleaned catalog sample only. The dot dashed line is the best fit of Just et al. (2007). The  $\alpha_{\text{ox}}$  in these plots are obtained by fitting photometric data points rather than from spectra. The typical error bar is displayed at the upper right corner.

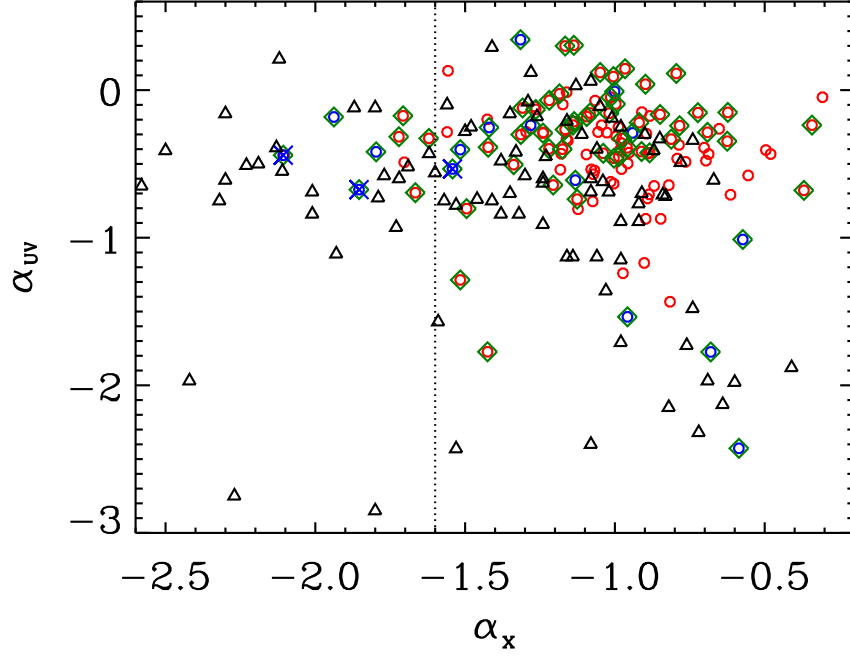


Fig. 16.— The relation between  $\alpha_{UV}$  and  $\alpha_x$ . Objects are selected from the clean catalog sample (open circles), excluding objects with fixed values of  $\alpha_x$ . The 17 low-redshift ( $z < 0.4$ ) objects are colored in blue and the remaining objects with  $z > 0.4$  are in red. NLS1s are marked with a cross on top of circles. We plot green open diamonds on top of low luminosity quasars with  $\log L_{2500 \text{ \AA}} < 30.5$ . For comparison, we also plot the AGN sample from Grupe et al. (2010) (open triangles). The vertical dotted line marks the position where  $\alpha_x = -1.6$ . The Spearman correlation coefficient for all objects from the clean catalog is  $\rho_s = 0.14$  ( $P_0 = 0.125$ ) which does not indicate significant correlation. The correlation coefficient for low redshift objects is  $\rho_s = 0.47$  ( $P_0 = 0.058$ ), for objects with  $\alpha_x > -1.6$  it is  $\rho_s = 0.22$  ( $P_0 = 0.017$ ) and for low luminosity quasars it is  $\rho_s = -0.04$  ( $P_0 = 0.726$ ).

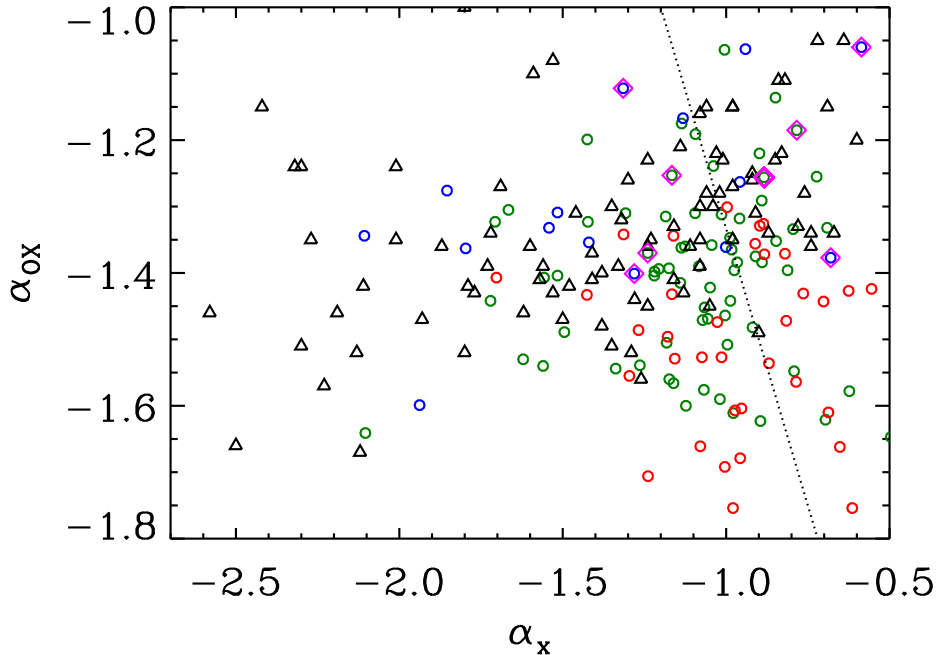


Fig. 17.— The relation between  $\alpha_{\text{ox}}$  and  $\alpha_{\text{x}}$  for 129 objects (open circles), selected from the clean catalog sample, excluding objects whose X-ray spectral indices are fixed during the fitting process or without  $L_{2500 \text{ \AA}}$  measured from UVOT photometry. Data points are color-coded depending on redshift with  $z < 0.4$  in blue,  $0.4 < z < 1.5$  in green and  $z > 1.5$  in red. Objects with  $L_{2500 \text{ \AA}} < 30.5$  are flagged with larger diamonds in magenta. The correlation coefficient of objects in our work is  $\rho_s = -0.06$  ( $P_0 = 0.484$ ), which does not exhibit a significant correlation (though with low confidence level). The dotted line is the weak correlation found by Young et al. (2009). For comparison, we over plot the G10 sample in open triangles.

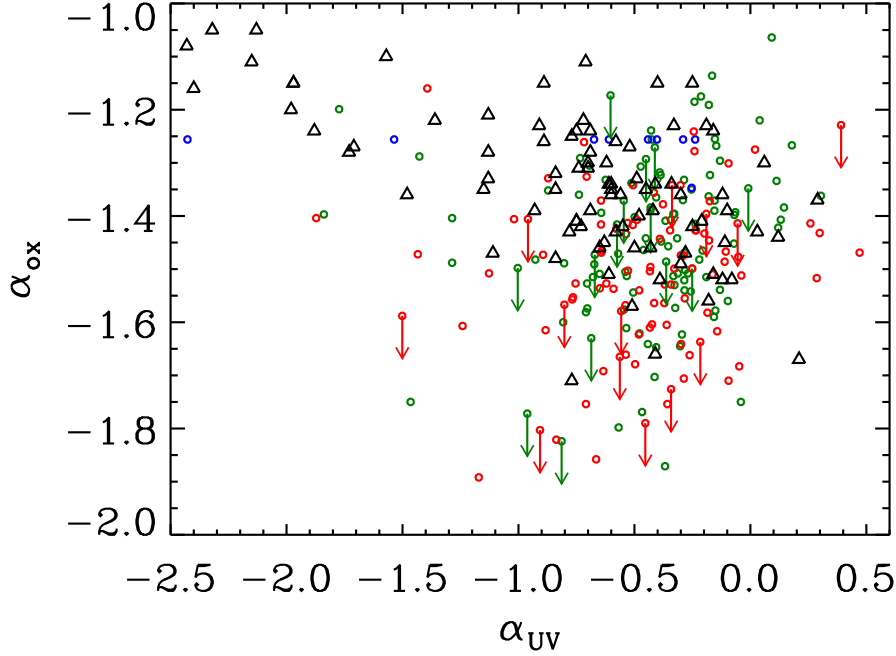


Fig. 18.— The relation between the UV/optical spectral index  $\alpha_{UV}$  and  $\alpha_{ox}$  for 217 objects, selected from the clean catalog sample, excluding objects whose  $L_{2\text{ keV}}$  is not available or without  $L_{2500\text{ \AA}}$  measured from UVOT photometry. Data points are color-coded in the same way as Fig. 17. The correlation coefficient of objects in our work is  $\rho_s = -0.17$ , which does not exhibit a significant correlation. Arrows represent quasars not detected by XRT. The low redshift ( $z < 0.4$ ) quasars in the clean catalog sample are color-coded in blue.

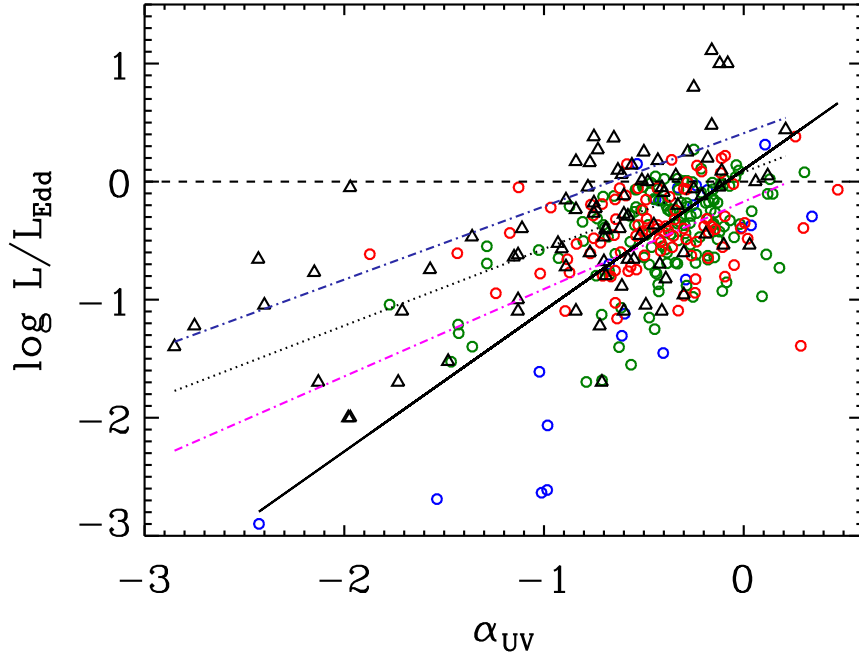


Fig. 19.— The relation between the Eddington ratio  $L_{\text{bol}}/L_{\text{Edd}}$  and the UV/optical spectral index  $\alpha_{\text{UV}}$  for 247 objects selected from the clean catalog sample, excluding objects with no bolometric luminosity measurements. Data points are color-coded in the same way as Fig. 17. The correlation coefficient of objects in our work is  $\rho_s = 0.35$  ( $P_0 < 10^{-3}$ ). The solid straight line is the best linear fit to our data by the BCES method. For comparison, we also plot the linear regression results of the BLS1, NLS1 AGNs and the combine of them obtained by Grupe et al. (2010) in magenta dash-dotted, blue dash-dotted and dotted lines, respectively.



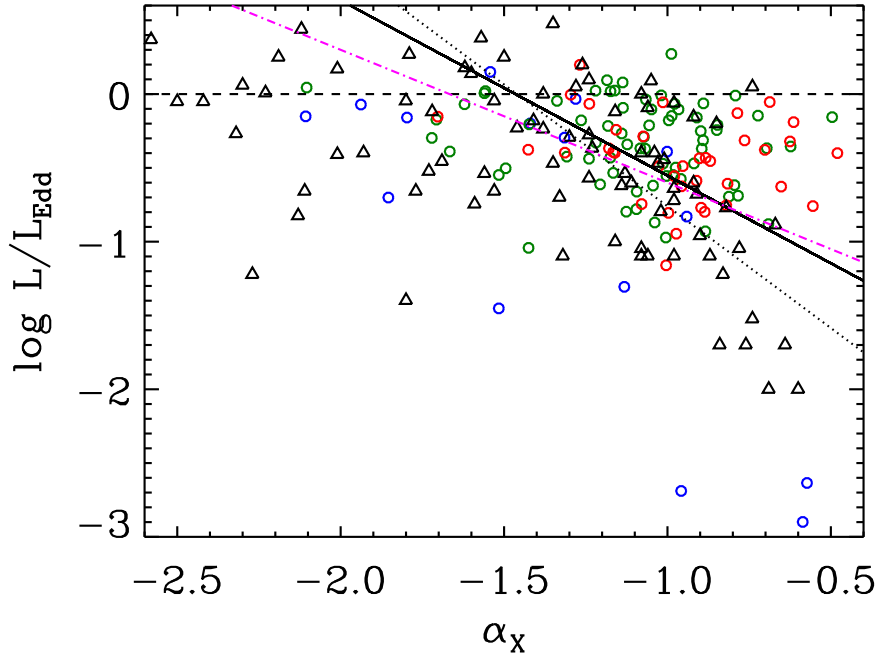


Fig. 20.— The relation between  $L_{\text{bol}}/L_{\text{Edd}}$  and  $\alpha_x$  for 129 objects selected from the clean catalog sample, excluding objects with fixed values of photon indices. Data points are color-coded in the same way as Fig. 17. The AGNs from Grupe et al. (2010) are represented with black open triangles. The correlation coefficient of objects in our work is  $\rho_s = -0.26$  ( $P_0 < 10^{-3}$ ). The solid black, dotted and dash-dotted lines represent the linear regression results to our sample, the G10 sample and the Shemmer et al. (2008) sample.

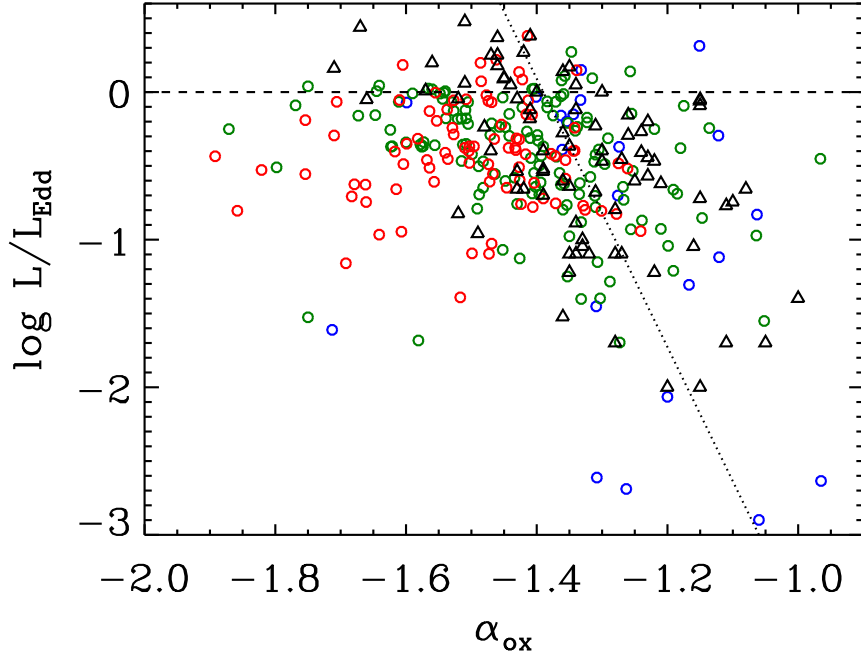


Fig. 21.— The relation between the Eddington ratio  $L_{\text{bol}}/L_{\text{Edd}}$  and  $\alpha_{\text{ox}}$  for 247 objects selected from the clean catalog sample, excluding objects whose  $\alpha_{\text{ox}}$  values are unavailable. Data points are color-coded in the same way as Fig. 17. The AGNs from Grupe et al. (2010) are represented with black open triangles. The dotted line is the linear regression result by Grupe et al. (2010).

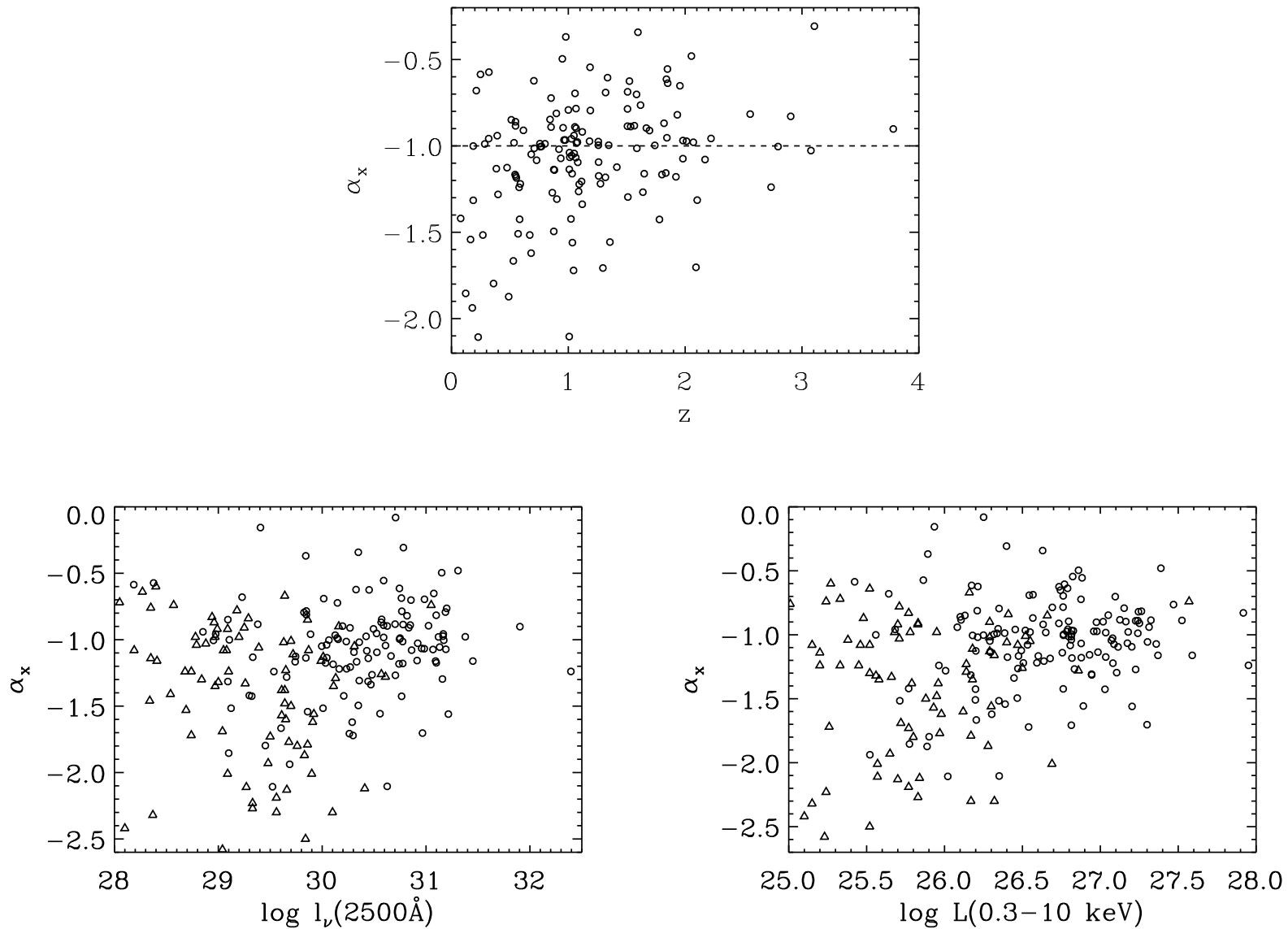


Fig. 22.— X-ray slope  $\Gamma$  vs. redshift (upper panel),  $L_{2500\text{\AA}}$  (lower left), and  $L_{2\text{ keV}}$  (lower right). In each panel, open circles represent data points in the clean catalog sample. Objects whose X-ray slopes are fixed during the fitting process are excluded. Open triangles represent data points in the G10 sample.

TABLE 1  
XRT DATA BINNING STRATEGY.

$N_{\text{Xph}}$	Photon# per Bin	Statistics	Flag
$N_{\text{Xph}} \geq 200$	20	$\chi^2$	$g(\text{good})$
$100 \leq N_{\text{Xph}} < 200$	$N_{\text{Xph}}/10$	$\chi^2$	$g(\text{good})$
$10 \leq N_{\text{Xph}} < 100$	1	Cash	$a(\text{acceptable})$
$N_{\text{Xph}} < 10$	Group Min 1 <sup>1</sup>	- <sup>2</sup>	$w(\text{weak})$
$N_{\text{Xph}} \sim 0$	...	...	$o(\text{Out of FOV})$

<sup>1</sup>In these cases, we group spectral bins with a minimum of 1 photon per bin.

<sup>2</sup>If the total number of X-ray photons is less than 10, we do not fit the X-ray spectrum but only calculate flux or flux limit.

TABLE 2  
MODELS USED TO FIT XRT SPECTRA.

Model	$\alpha_x$	$N_{H,i}$	Objects	Percentage
A	Fixed to $-1$	Fixed to 0	177	44%
B	Free	Fixed to 0	195	49%
C	Free	Free	15	4%
D	Fixed to $-1$	Free	12	3%

TABLE 3  
 UVOT SKY IMAGE FLAGGING DESCRIPTION.

Flag	Description	Source Region	Background Region
-2	Bad Aspect	None	None
-1	Out of Image	None	None
1	Faint	Default	Default
0	$\delta \leq 0''.618$	Default <sup>a</sup>	Default <sup>a</sup>
2	$0''.618 < \delta \leq 3''$	Customized <sup>b</sup>	Default <sup>a</sup>
3	$\delta > 3''$	None	None
4	Near edge ( $d_E \leq 27''.5$ )	None	None
5	Not in FOV	None	None
10+	$27''.5 < d_E \leq 35''$	TBD <sup>c</sup>	TBD <sup>c</sup>
100+	$d_V \leq 100''$	TBD <sup>c</sup>	TBD <sup>c</sup>

NOTE.— $\delta$  is the separation between the SDSS coordinate and the Gaussian centroid resulting from fitting the object image (see Section 2.3);  $d_E$  is the distance between the source position and the sky image edge;  $d_V$  is the distance between the source position and the nearest vertex of a sky image.

<sup>a</sup>See Section 2.3 for descriptions of the default source and background region files.

<sup>b</sup>Source region circles are centered at the new Gaussian centroid.

<sup>c</sup>These images are passed to the visual inspection process (Section 2.3)

TABLE 4  
FOUR TYPES OF OBJECTS IN THE RAW CATALOG.

Type	UVOT	XRT	In Catalog	SED	Number
A	Y	Y	Y	Y	637
B	Y	N	Y	N	38
C	N	Y	Y	N	168
D	N	N	N	N	191
Total	675	805	843	637	1034

TABLE 5  
PHOTOMETRIC SHIFT STRATEGIES.

Priority <sup>1</sup>	UV Bands Condition	EUV Bands Condition	Method <sup>2</sup>
1	$g+u+U$		E
2		$g+u+U$	E
3	$g+B+u$		I
4		$g+B+u$	I
5	$r+g+B$		E
6	$r+V+g$		I
7		$r+V+g$	I
8	$V+u+g$		E
9	$i+r+V$	$i+r+V$	E
10	$g+u+UVW1$		E
11		$g+u+UVW1$	E
12	$g+u+UVM2$		E
13	$g+u+UVW2$		E
14		$g+u+UVW2$	E
15		$g+u+UVM2$	E

<sup>1</sup>The highest priority is 1.

<sup>2</sup>E for extrapolation; I for interpolation



TABLE 6  
PARAMETERS FOR BLACK HOLE MASS CALCULATION.

Redshift	FWHM	$\lambda_c^a$	$a$	$b$	BC	Reference
$z < 0.7$	FWHM(H $\beta$ )	5100 Å	0.660	0.53	9.26	McLure & Dunlop (2004)
$0.7 < z < 1.9$	FWHM(Mg II)	3000 Å	0.505	0.62	5.15	McLure & Jarvis (2002); McLure & Dunlop (2004)
$z > 1.9$	FWHM(C IV)	1350 Å	0.672	0.61	3.81	Vestergaard & Peterson (2006)

<sup>a</sup>Wavelength of continuum monochromatic luminosity.

TABLE 7  
CATALOG DESCRIPTION.

Column	Format	Symbol	Description
1	A18	SDSSID	SDSS DR5 Designation hhmss.ss+ddmss.s(J2000)
2	F10.6	RA	SDSS right ascension in decimal degrees (J2000)
3	F10.6	DEC	SDSS declination in decimal degrees (J2000)
4	F6.4	$z$	Redshift from SDSS DR5 quasar catalog
5	F6.2	$M_i$	Absolute magnitude at $i$ band from SDSS DR5 quasar catalog
6	F6.3	$u$	BEST PSF $u$ magnitude (not corrected for Galactic extinction)
7	A1	Quality Flag	Data quality ( $a/b/c/d$ )
8	I1	Catalog Flag	1 =in final catalog, 0 =not in final catalog
9	I1	SED	1 =has SED plots, 0 =no SED plot
10	I1	$N_{2\text{MASS}}$	Number of 2MASS photometric points
11	I1	$N_{\text{UVOT}}$	Number of UVOT photometric data points
12	A1	XRT Flag	Quality of XRT data ( $g/a/w/o$ )
13	A6	QSO Type	Classification of quasar
14	A1	XRT Model	Model used to fit XRT spectrum ( $a/b/c/d$ )
15	I2	Red Flag	1 =color is "red", 0 =color is not red
16	I1	SDSS Fit	1 =SDSS spectrum is fit, 0 =SDSS spectrum is not fit
17	F7.3	$\Gamma$	Photon index between 0.3 and 10 keV
18	F7.3	$\delta^- (\Gamma)$	$1\sigma$ lower error bar of photon index
19	F7.3	$\delta^+ (\Gamma)$	$1\sigma$ upper error bar of photon index
20	F7.3	HR	Hardness ratio <sup>3</sup>
21	F7.3	$\log F_{\text{obs}}(0.3\text{--}10 \text{ keV})$	Observed flux between 0.3 and 10 keV
22	F7.3	$\log F_{\text{unobs}}(0.3\text{--}10 \text{ keV})$	Unabsorbed flux between 0.3 and 10 keV
23	F7.3	$\log L_2 \text{ keV}$	Monochromatic luminosity at 2 keV in $\text{erg s}^{-1} \text{ Hz}^{-1}$ in logarithmic scale
24	F7.3	$\delta \log L_2 \text{ keV}$	$1\sigma$ uncertainty of monochromatic luminosity at 2 keV
25	F7.3	$\log L(0.3\text{--}10 \text{ keV})$	Integrated luminosity between 0.3 and 10 keV in $\text{erg s}^{-1}$
26	I2	XRT Detect	1 =detection, 0 =non-detection, -1 =not observed
27	E9.2	CR	Source count rate in $10^{-3} \text{ cnt s}^{-1}$
28	F8.1	$T_{\text{XRT}}$	Total XRT exposure time in seconds
29	F5.3	$N_{\text{H,G}}$	Galactic column density in $10^{20} \text{ cm}^{-2}$
30	F7.3	$N_{\text{H,i}}$	Intrinsic column density in $10^{22} \text{ cm}^{-2}$
31	F7.3	$\delta_- (N_{\text{H,i}})$	$1\sigma$ lower error bar in $10^{22} \text{ cm}^{-2}$ of $N_{\text{H,i}}$
32	F7.3	$\delta_+ (N_{\text{H,i}})$	$1\sigma$ upper error bar in $10^{22} \text{ cm}^{-2}$ of $N_{\text{H,i}}$
33	I2	V Flag	1 =has V band photometry, -1 =no V band photometry
34	F8.1	$T_V$	Total exposure time (seconds) in V band
35	F7.3	$\log f(V)$	Flux density at <i>Swift</i> V band <sup>1</sup>
36	F7.3	$\delta \log f(V)$	$1\sigma$ error bar of flux density at <i>Swift</i> V band
37	I2	B Flag	1 =has B band photometry, -1 =no B band photometry
38	F7.1	$T_B$	Total exposure time (seconds) in B band
39	F7.3	$\log f(B)$	Flux density at <i>Swift</i> B band <sup>1</sup>
40	F7.3	$\delta \log f(B)$	$1\sigma$ error bar of flux density at <i>Swift</i> B band
41	I2	U Flag	1 =has U band photometry, -1 =no U band photometry
42	F7.1	$T_U$	Total exposure time (seconds) in U band
43	F7.3	$\log f(U)$	Flux density at <i>Swift</i> U band <sup>1</sup>
44	F7.3	$\delta \log f(U)$	$1\sigma$ error bar of flux density at <i>Swift</i> U band
45	I2	UVW1 Flag	1 =has UVW1 band photometry, -1 =no UVW1 band photometry
46	F8.1	$T_{\text{UVW1}}$	Total exposure time (seconds) in UVW1 band
47	F7.3	$\log f(\text{UVW1})$	Flux density at <i>Swift</i> UVW1 band <sup>1</sup>
48	F7.3	$\delta \log f(\text{UVW1})$	$1\sigma$ error bar of flux density at <i>Swift</i> UVW1 band
49	I2	UVM2 Flag	1 =has UVM2 band photometry, -1 =no UVM2 band photometry
50	F8.1	$T_{\text{UVM2}}$	Total exposure time (seconds) in UVM2 band
51	F7.3	$\log f(\text{UVM2})$	Flux density at <i>Swift</i> UVM2 band <sup>1</sup>
52	F7.3	$\delta \log f(\text{UVM2})$	$1\sigma$ error bar of flux density at <i>Swift</i> UVM2 band
53	I2	UVW2 Flag	1 =has UVW2 band photometry, -1 =no UVW2 band photometry
54	F8.1	$T_{\text{UVW2}}$	Total exposure time (seconds) in UVW2 band

TABLE 7—*Continued*

Column	Format	Symbol	Description
55	F7.3	$\log f(\text{UVW2})$	Flux density at <i>Swift</i> UVW2 band <sup>1</sup>
56	F7.3	$\delta \log f(\text{UVW2})$	1 $\sigma$ error bar of flux density at <i>Swift</i> UVW2 band
57	F7.3	$\alpha_{\text{UV,ph}}$	UV spectral index by fitting photometric data
58	F7.3	$\delta \alpha_{\text{UV,ph}}$	1 $\sigma$ error bar of $\alpha_{\text{UV,ph}}$
59	F7.3	$\log L_{2500 \text{ \AA}}$	$\log L_{2500 \text{ \AA}}$ by fitting UV photoemtric data in $\text{erg s}^{-1} \text{ Hz}^{-1}$
60	F7.3	$\delta \log L_{2500 \text{ \AA}}$	1 $\sigma$ error bar of $\log L_{2500 \text{ \AA}}$
61	F7.3	$\alpha_{\text{ox,ph}}$	$\alpha_{\text{ox}}$ calculated using $\log L_{2500 \text{ \AA}}$ and $\log L_2 \text{ keV}$
62	F7.3	$\delta \alpha_{\text{ox,ph}}$	1 $\sigma$ error bar of $\alpha_{\text{ox,ph}}$
63	F7.3	$\log M_{\text{BH}}$	Black hole mass <sup>2</sup>
64	F7.3	$\log L_{\text{bol,EXP}}$	Bolometric luminosity by the EXP model in $\text{erg s}^{-1}$
65	F7.3	$\log L_{\text{bol,TPL}}$	Bolometric luminosity by the TPL model in $\text{erg s}^{-1}$

NOTE.—Data entry is usually set to  $-99.9$  if unavailable.

<sup>1</sup>Fluxes are in  $10^{-17} \text{ erg s}^{-2} \text{ cm}^{-2} \text{ \AA}^{-1}$ , and are corrected for Galactic reddening.

<sup>2</sup>Calculated using emission line FWHM and corresponding continuum flux calculated by power-law fitting of photometric data points.

<sup>3</sup>The hardness ratio here is defined as  $(N_{\text{H}} - N_{\text{S}})/(N_{\text{H}} + N_{\text{S}})$ , in which  $N_{\text{H}}$  is the X-ray photon count between 1 and 10 keV and  $N_{\text{S}}$  is the X-ray photon count between 0.3 and 1 keV.

TABLE 8  
DATA OF SELECTED CATALOG COLUMNS FOR OBJECT EXAMPLES.

SDSSID	$z$	Quality Flag	XRT Flag	XRT Model	$\Gamma$	$\log L_2$ keV [erg s <sup>-1</sup> Hz <sup>-1</sup> ]	XRT Detect	$N_{\text{H},i}$ [10 <sup>22</sup> cm <sup>-2</sup> ]	$\alpha_{\text{UV,ph}}$	$\log L_{2500 \text{ \AA}}$ [erg s <sup>-1</sup> Hz <sup>-1</sup> ]	$\alpha_{\text{ox}}$
000639.20 + 142156.1	1.3920	A	a	d	2.000	27.187 ± 0.096	1	2.517 <sup>+1.424</sup> <sub>-1.054</sub>	-0.927 ± 0.013	31.049 ± 0.002	-1.482 ± 0.037
000654.40 + 141442.7	1.6359	C	w	...	...	28.411	0	0.000	...	...	...
001141.40 - 004722.6	1.6483	A	w	...	...	27.050	0	0.000	0.083 ± 0.142	30.086 ± 0.032	-1.160
001217.08 - 005437.6	3.6030	C	w	...	...	28.490	0	0.000	...	...	...
001746.50 - 093546.1	0.5790	A	a	b	2.240 <sup>+0.238</sup> <sub>-0.220</sub>	25.964 ± 0.062	1	0.000	-0.291 ± 0.060	29.535 ± 0.013	-1.370 ± 0.024
001904.83 + 003436.5	2.1178	A	w	...	...	30.320	0	0.000	-0.290 ± 0.073	30.976 ± 0.011	-0.250
001917.31 + 002735.4	2.4183	C	a	a	2.000	27.202 ± 0.152	1	0.000	...	...	...
001927.17 + 003539.0	1.2889	A	a	a	2.000	26.588 ± 0.114	1	0.000	-0.673 ± 0.089	30.472 ± 0.013	-1.491 ± 0.044
001927.87 + 003359.9	1.6234	A	w	...	...	26.936	0	0.000	...	...	...
001954.60 + 004114.1	1.9081	A	w	...	...	26.988	0	0.000	-0.959 ± 0.297	30.652 ± 0.058	-1.406
001957.60 + 003936.2	0.9945	A	a	a	2.000	26.472 ± 0.092	1	0.000	-0.513 ± 0.074	29.959 ± 0.014	-1.338 ± 0.036
002303.15 + 011533.6	0.7285	A	g	b	2.083 <sup>+0.162</sup> <sub>-0.154</sub>	26.807 ± 0.044	1	0.000	-0.155 ± 0.046	30.430 ± 0.010	-1.390 ± 0.017
002740.38 + 010608.6	1.5062	A	a	a	2.000	26.192 ± 0.181	1	0.000	0.471 ± 0.157	30.021 ± 0.031	-1.469 ± 0.070
002828.34 - 011014.1	1.1930	A	w	...	...	26.595	0	0.000	-0.370 ± 0.106	30.378 ± 0.017	-1.452
003359.38 + 000230.0	1.6367	C	w	...	...	27.870	0	0.000	...	...	...
003409.08 + 000318.4	1.2015	A	w	...	...	26.621 ± 0.288	1	0.000	-0.039 ± 0.051	30.208 ± 0.008	-1.377 ± 0.111
003415.77 - 000030.8	1.9451	A	w	...	...	26.940	0	0.000	...	...	...
003431.78 - 000957.4	1.5043	A	a	a	2.000	26.823 ± 0.138	1	0.000	-0.566 ± 0.156	30.444 ± 0.028	-1.390 ± 0.054
003435.13 - 000947.8	1.6711	A	w	...	...	26.995	0	0.000	-0.338 ± 0.155	30.450 ± 0.023	-1.326
003922.44 + 005951.7	1.9889	A	w	...	...	26.879 ± 0.391	1	0.000	-0.463 ± 0.288	30.723 ± 0.040	-1.475 ± 0.150
003940.23 + 004241.5	1.7010	B	o	...	...	...	-1	...	0.037 ± 0.040	30.117 ± 0.009	...
005446.22 + 140019.0	0.5015	A	g	a	2.000	25.019 ± 0.089	1	0.000	-1.465 ± 0.220	29.577 ± 0.040	-1.750 ± 0.038
005503.52 + 140806.5	1.6679	A	g	c	1.897 <sup>+0.143</sup> <sub>-0.151</sub>	27.164 ± 0.077	1	0.647 <sup>+0.372</sup> <sub>-0.337</sub>	-0.872 ± 0.086	30.626 ± 0.019	-1.329 ± 0.030
011056.90 + 001912.0	0.8056	A	w	...	...	26.837	0	0.000	-0.412 ± 0.016	30.149 ± 0.003	-1.271
011119.81 + 002652.0	1.7475	A	a	a	2.000	27.005 ± 0.098	1	0.000	-0.234 ± 0.088	30.724 ± 0.013	-1.427 ± 0.038
011124.42 + 002647.0	1.0029	A	a	a	2.000	26.402 ± 0.105	1	0.000	-0.285 ± 0.061	30.365 ± 0.012	-1.521 ± 0.041
113749.11 + 404913.5	1.1886	A	a	b	1.795 <sup>+0.233</sup> <sub>-0.226</sub>	26.350 ± 0.069	1	0.000	0.113 ± 0.110	29.825 ± 0.018	-1.334 ± 0.027
114502.23 + 595720.0	1.6385	A	g	b	2.268 <sup>+0.065</sup> <sub>-0.063</sub>	26.834 ± 0.019	1	0.000	-0.111 ± 0.045	30.705 ± 0.009	-1.486 ± 0.008
145353.56 + 032450.8	2.4045	A	a	a	2.000	26.965 ± 0.128	1	0.000	-0.415 ± 0.001	31.041 ± 0.000	-1.564 ± 0.049
154929.43 + 023701.1	0.4144	A	g	b	1.719 <sup>+0.024</sup> <sub>-0.024</sub>	27.075 ± 0.009	1	0.000	-0.741 ± 0.079	29.948 ± 0.015	-1.103 ± 0.007
165004.94 + 313354.6	1.6948	A	g	c	1.911 <sup>+0.271</sup> <sub>-0.276</sub>	26.734 ± 0.127	1	0.772 <sup>+0.688</sup> <sub>-0.552</sub>	-0.416 ± 0.075	30.268 ± 0.016	-1.356 ± 0.049

NOTE.—Refer to Table 7 for conventions of notations and meanings of flags. Values without error bars are usually because they are fixed (e.g.,  $\Gamma$  and  $N_{\text{H},i}$ ) or they represent upper limits (e.g.,  $\alpha_{\text{ox}}$  and  $\log L_2$  keV). Entries without values are because they cannot be measured. The complete catalog content is published in its entirety in the electronic version of the *Astrophysical Journal Supplement*. The portion is shown here for guidance regarding its form and content.

TABLE 9  
 QUASAR TYPES EXCLUDED FROM CLEAN CATALOG SAMPLE.

Classification	Objects
BAL quasar	50
BL Lac	1
Lensed quasar	2
Extended	1
RL	97
Sy 1.8	1
Dust reddened	50

NOTE.—Classifications  
 may overlap.

TABLE 10  
SAMPLE SELECTION AND PROPERTIES.

Sample	Catalog	G10	Total
Parent Sample	637	88 <sup>1</sup>	725
Small Clean Sample	214	88	302
X-ray Detection Rate	85%	100%	89%
Large Clean Sample	426	88	514
X-ray Detection Rate	65%	100%	71%

<sup>1</sup>The sample in Grupe et al. (2010) contains 92 objects, but 4 objects do not have UVOT observations.

TABLE 11  
CORRELATION AND REGRESSION ANALYSIS.

Sample	Size	$\rho_s(P_0)^3$	EM			BJ		
			Slope	Intercept	Dispersion <sup>1</sup>	Slope	Intercept	Dispersion <sup>2</sup>
Small clean catalog	207	-0.55	$-0.156 \pm 0.022$	$3.244 \pm 0.676$	0.122	$-0.157 \pm 0.022$	3.276	0.115
Small clean catalog+G10	295	-0.68	$-0.140 \pm 0.014$	$2.773 \pm 0.420$	0.113	$-0.142 \pm 0.013$	2.830	0.107
Big clean catalog	426	-0.47	$-0.148 \pm 0.013$	$3.018 \pm 0.398$	0.148	$-0.146 \pm 0.013$	2.972	0.140
Big clean catalog+G10	514	-0.57	$-0.125 \pm 0.008$	$2.338 \pm 0.246$	0.140	$-0.126 \pm 0.008$	2.355	0.131
J07	372	-0.76	$-0.140 \pm 0.007$	$2.704 \pm 0.212$	0.150	$-0.140 \pm 0.006$	2.723	0.132
J07T <sup>4</sup>	289	-0.66	$-0.134 \pm 0.010$	$2.541 \pm 0.310$	0.154	$-0.137 \pm 0.009$	2.612	0.132

NOTE.—EM: Expectation-Maximization algorithm; BJ: Buckley-James algorithm.

<sup>1</sup>Standard normal residual. See Lavalley et al. (1992).

<sup>2</sup>Kaplan-Meier residual. See Lavalley et al. (1992).

<sup>3</sup>Spearman rank correlation coefficient  $\rho_s$  with confidence level  $P_0$ .

<sup>4</sup>J07 sample after excluding high luminosity quasars with  $\log l_\nu(2500 \text{ \AA}) > 31.5$ .